Loss of PIMREG impairs double-strand break signaling and repair

Maria Vitória de Rizzo Gasparini[1,a]; Laís do Carmo[1,a]; Giovanna Gonçalves de Almeida[1]; Mariana Siqueira Lacerda Mamede[1]; Isabela Spido Dias[1]; Jennifer Ann Black[1,2]; Vanessa Cristina Arfelli[3]; Yun-Chien Chang[4]; Stephanie Heinzlmeir[4]; Bernhard Kuster[4], Philipp A. Greif[3,5,6]; Leticia Fröhlich Archangelo[1,*]

[1] Department of Cellular and Molecular Biology and Pathogenic Bioagents, Ribeirão Preto Medical School, University of São Paulo (FMRP-USP), Ribeirão Preto, São Paulo, Brazil.

[2] University of Glasgow Centre for Parasitology, School of Infection and Immunity, Sir Graeme Davies Building, 120 University Place, Glasgow, G12 8TA, United Kingdom

[3] Laboratory for Experimental Leukemia and Lymphoma Research, Munich University Hospital, Ludwig-Maximilians University (LMU), Munich, Germany

[4] Chair of Proteomics and Bioanalytics, School of Life Sciences Weihenstephan, Technical University of Munich (TUM), Freising, Germany

[5] German Cancer Consortium (DKTK), partner site Munich

[6] German Cancer Research Center (DKFZ), Heidelberg, Germany

[a] These authors contributed equally to this work

[*]Corresponding Author: Leticia Fröhlich Archangelo

Department of Cellular and Molecular Biology and Pathogenic Bioagents, Ribeirão Preto Medical School, University of São Paulo,

Av Bandeirantes 3900, 14049-900 Ribeirão Preto-SP, Brazil. Tel: +55 (16) 33153118; fax: + 55 (16) 3315 0728

E-mail: leticiafa@fmrp.usp.br (L.F. Archangelo)

Abstract

Glioblastoma (GBM) is the most common primary brain tumor in adults. It is an aggressive type of tumor with an average overall survival of 12-15 months post-diagnosis. Standard treatment involves surgical resection, followed by radiotherapy and chemotherapy with temozolomide (TMZ). However, resistance to treatment is frequently observed. PIMREG is a marker of proliferation highly expressed across different tumor types, with particularly elevated levels in GBM. Our previous study revealed that PIMREG silencing sensitizes GBM cells to TMZ treatment and affects ATM activation, a key apical kinase involved in DNA damage signaling. Given the emerging significance of PIMREG in DNA damage response, we sought to explore PIMREG's role in DNA damage repair and signaling in GBM cells exposed to genotoxic agents. Here we assessed the functionally enriched pathways associated with high *PIMREG* expression in GBM patient samples, analyzed the interactome of PIMREG upon treatment of GBM cells with TMZ and evaluated the impact of PIMREG on DNA damage signaling alongside its function in the repair of double-strand breaks. Our findings reveal that PIMREG functions as a direct substrate for ATM/ATR kinases, interacts with key DNA repair proteins upon TMZ treatment and actively facilitates the cellular response to chemotherapy- and radiotherapy-induced DNA damage. Taken together, PIMREG may function during DNA damage signaling, specifically during the repair of double strand breaks via homologous recombination in GBM cells. In all, our data suggested high PIMREG expression may contribute to the resistance of GBM cells to treatment.

Key Words: CATS, FAM64A, GBM, DSBs, HR, TMZ, IR

52 **1. Introduction**

53 Diffuse gliomas are the most common primary malignant brain tumors [1]. Among gliomas,
54 GBM grade 4 is the most aggressive subtype, characterized by rapid progression and poor
55 prognosis [2,3]. The median survival time for patients with GBM is approximately 12 to 15
56 months following diagnosis, with a 5-years survival rate of 9.8 % [4]. The standard
57 treatment consists of surgical resection followed by radiotherapy with ionizing irradiation
58 (IR) and chemotherapy with TMZ [5].

59 Treatment with IR and TMZ is based on inducing DNA damage in tumor cells, which
60 promotes cytotoxicity and cell death. Whereas IR mostly induces double-strand breaks
61 (DSBs) in the DNA through radiolysis and formation of reactive oxygen species (ROS) [6],
62 TMZ primarily alkylates DNA bases. O6-methylguanine (O6-MeG) is the most cytotoxic
63 lesion and is repaired by the direct repair mechanism mediated by the O6-methylguanine-
64 DNA methyltransferase (MGMT) [7]. Thus, hypermethylation of the promoter region of
65 the *MGMT* gene predicts response to TMZ treatment [8]. In this scenario, inefficient repair
66 of O6-MeG leads to futile cycles of mismatch repair (MMR), replication fork collapse and
67 ultimately DSB formation [9].

68 DSBs are highly cytotoxic DNA lesions that threaten genome stability if unresolved. In
69 response, eukaryotic organisms possess a multitude of pathways orchestrated through a
70 network of proteins to tackle these severe lesions. DSBs however, are primarily resolved
71 through the activation of two main pathways: homologous recombination (HR) [10] and
72 non-homologous end joining (NHEJ) [11]. Overcoming DSB lesions through DNA repair
73 is a critical mechanism for acquiring resistance to therapy. In fact, elevated activities of HR
74 and NHEJ are observed in patient-derived GBM samples with acquired TMZ resistance,
75 suggesting that these pathways play a central role in the development of treatment
76 resistance [12].

77 PICALM-interacting mitotic regulator (*PIMREG*) plays a well-established role in cell cycle
78 progression, specifically in proliferation and chromosome segregation during cell division
79 [13–15]. Additional functions have been proposed for PIMREG in the developing central
80 nervous system (CNS) [13], cell differentiation [15–17], fetal cardiomyocyte cell cycle
81 progression [18,19], and in signaling pathways such as JAK-STAT3 [17], NF-κB [20], and
82 β-catenin [21,22]. PIMREG expression levels strongly correlate with cellular proliferation
83 in both normal and malignant cells [13].
84 The contribution of PIMREG in promoting malignant phenotypes has been primarily
85 addressed in breast cancers, where multiple functional studies have linked PIMREG to cell
86 migration, metastasis, epithelial-mesenchymal transition, enhanced stemness features, and
87 aggressiveness of breast cancer cells [20,22,23]. In another hormone-sensitive cancer, such
88 as prostate cancer (PCa), PIMREG was described as an oncogenic factor whose expression
89 became activated through direct binding of the androgen receptor (AR) to the *PIMREG*
90 promoter, leading to proliferation, colony formation, migration, invasion, and cell cycle
91 progression of PCa cells [24].
92 The oncogenic role of PIMREG in cancer development has been shown *in vivo* by three
93 elegant studies. Jiang and colleagues demonstrated that overexpression of PIMREG
94 promotes breast cancer aggressiveness via constitutive activation of NF-κB signaling
95 pathway. Mechanistically, PIMREG overexpression sustains constitutive activation of NF-
96 κB signaling by competing with IkB for interaction, thereby disrupting the NF-κB/IκBα
97 negative feedback loop. In cells expressing high levels of PIMREG, such as breast cancer
98 cells, PIMREG interacts with the p65 subunit of NF-κB within the nucleus, thereby
99 stabilizing p65, and enhancing its binding to NF-κB response elements, promoting
100 activation of its target genes and consequently hyperactivation of NF-κB signaling that
101 correlates with cancer development and progression [20].

102 The PIMREG-mediated activation of the NF-κB pathway is also implicated in promoting
103 cisplatin resistance in triple-negative breast cancer (TNBC) both *in vivo* and *in vitro* [25].
104 For instance, SOD1-high fibroblasts produce exosomal miR-3960 that targets the kinase
105 BRSK2 in TNBC cells. BRSK2 is responsible for phosphorylating PIMREG at Ser16
106 leading to PIMREG ubiquitination and subsequent degradation. Due to miR-3960-mediated
107 downregulation of BRSK2 , PIMREG Ser16 phosphorylation becomes reduced thereby
108 increasing protein stability. Consequently, NF-κB signaling is activated correlating with
109 cisplatin resistance in TNBC cells. Conversely, decreased PIMREG levels due its
110 phosphorylation of Ser16, enhances cisplatin sensitivity in TNBC cells [25].
111 In a third study, Xu and colleagues revealed PIMREG's critical role in inflammation-
112 associated tumorigenesis. Mice lacking *Pimreg* exhibited impaired differentiation of Th17
113 lymphocytes, leading to reduced proinflammatory activity typically associated with these
114 cells. PIMREG is essential for IL-6–mediated activation of STAT3 and regulates Th17 cell
115 differentiation by modulating STAT3 transcriptional activity. As a result, PIMREG plays a
116 key role in the development of Th17-driven inflammatory diseases, including autoimmune
117 encephalomyelitis, colitis and colitis-associated carcinogenesis in animal models [17].
118 Consistent with its role as a proliferation marker, *PIMREG* is highly expressed in tumor
119 tissues compared to normal tissue samples. Additionally, high expression of *PIMREG* in
120 patient samples correlated with worse prognosis and reduced overall survival across various
121 types of cancer [26,27]; including breast cancer [20,22,23,28]; pancreatic cancer [29]; lung
122 cancer [30]; prostate cancer [24]; head and neck squamous cell carcinoma [31]; clear cell
123 renal cell carcinoma [32]; gastric cancer [33]; melanoma [34] and gliomas [35].
124 We have previously shown that GBM exhibits the highest level of *PIMREG* expression
125 amongst 25 types of cancer. As well as showing that PIMREG silencing reduced malignant
126 characteristics of GBM cells, such as cell cycle progression, proliferation and migration

127 capacity, we demonstrated that treating these cells with TMZ increased the levels of
128 PIMREG protein. In addition, PIMREG silencing rendered GBM cells more sensitive to
129 TMZ exposure and interfered with ATM activation, a key apical kinase that orchestrates
130 the cellular response to DSBs. We hypothesized that PIMREG plays a role in DNA damage
131 response (DDR) and therefore could contribute to TMZ resistance [35].
132 The mechanism by which PIMREG participates in the DDR in GBM cells is unclear. To
133 begin addressing these knowledge deficits and gain further insight into PIMREG function
134 and relevance in GBM, we tested for functionally enriched pathways related to elevated
135 *PIMREG* expression in GBM patient samples and analyzed the correlation between
136 *PIMREG* expression and those of DDR-related genes. We investigated the interactome of
137 PIMREG upon treatment of GBM cells with TMZ and evaluated the impact of PIMREG
138 on DNA damage signaling alongside its function in the repair of DSBs. Our data reveal that
139 PIMREG interacts with proteins involved mainly in DDR and RNA metabolism following
140 TMZ treatment in GBM cells. Additionally, PIMREG serves as a substrate for ATM/ATR
141 and plays a role in DNA damage signaling and the repair of DSBs. These findings further
142 suggest the importance of elevated expression of PIMREG in GBM maintenance and its
143 possible contribution to the treatment resistance in GBM patients.
144
145

146 **2. Material and methods**

147 **2.1. Public data analysis**

148 GBM RNAseq-based mRNA expression (RSEM) data were downloaded from TCGA-
149 PanCancer Atlas_2018 (592 samples) using cBioPortal for Cancer Genomics [36].
150 Gene set enrichment analysis was performed using GSEA version 4.3.2 [37]. Results were
151 regarded as significant with a p-value < 0.05 and 25 % false discovery rate (FDR) threshold
152 (q-value <0.25).
153 Genes coding for DDR proteins, whose expression covariates with *PIMREG* in GBM patient
154 samples were plotted in a correlation curve using GraphPad Prism 9.
155 *PIMREG* mRNA expression data, along with *MGMT* promoter methylation status, were
156 also obtained from the merged cohorts of Brain Lower Grade Glioma (LGG) (TCGA,
157 PanCancer Atlas, 514 samples) and GBM (TCGA, PanCancer Atlas, 592 samples). Among
158 the 1106 available samples, 635 contained information regarding the methylation status of
159 the *MGMT* promoter.

160 **2.2. Cell lines**

161 The GBM human cell line T98G was obtained from the American Type Culture Collection
162 (ATCC, Manassas, USA) and U87MG from the Banco de Células do Rio de Janeiro (BCRJ,
163 Rio de Janeiro, Brazil). The reporter cell lines HeLa EJ5-GFP and U2OS DR-GFP were
164 kindly provided by Dr. Valeria Valente (School of Pharmaceutical Science, UNESP,
165 Brazil). The cells were cultured in Dulbecco's Modified Eagle's Medium (DMEM, Gibco)
166 supplemented with 10 % of fetal bovine serum (FBS, Gibco) and 1 % of the antibiotic
167 penicillin/streptomycin (Gibco), at 37 °C and 5 % of CO_2. All cell lines were tested for
168 mycoplasma with MycoAlert PLUS Mycoplasma Detection Kit (Lonza). T98G were
169 authenticated by STR matching analysis using the GenePrint 10 system (Promega,

170 Madison, WI, USA) and 3730 DNA Analyzer - Applied Biosystems (Applied Biosystems,
171 Foster City, CA, USA).

172 **2.3. Cell treatment with genotoxic agents**

173 Temozolomide (TMZ, Sigma-Aldrich # T2577 and Selleckchem S1237) were diluted in
174 DMSO at a stock concentration of 50 mM and 200 mM, respectively. Stocks were stored
175 in 500 µL aliquots at - 80 ºC.
176 GBM cells were treated with 300 µM TMZ or vehicle (DMSO) for 24 h, for Western blot
177 analysis, cell cycle, apoptosis, immunoprecipitation and immunofluorescence experiments.
178 For IR treatment, GBM cells were irradiated using the PRIMUS linear accelerator (Siemens
179 Healthineers, Brazil) with a 6 MV photon beam at the Hospital das Clínicas - Ribeirão Preto
180 Medical School. The administered dose was 4 Gy. Cells were collected 0.5 h and 1 h post-
181 irradiation for Western blot analysis and immunofluorescence experiments. The
182 concentration and time used for the TMZ and IR treatments were defined as such to induce
183 DNA damage signaling but not cell cycle arrest or apoptosis. Cell cycle progression and
184 viability were monitored in all GBM cell samples treated with genotoxic agents
185 (Supplementary Fig. S1C, S1D and Fig. S2D).

186 **2.4. Plasmid construction**

187 For genome editing, single guide RNAs (sgRNAs) targeting exon 2 of *PIMREG* were
188 designed using the Benchling CRISPR sgRNA design tool
189 (https://www.benchling.com/crispr). The 20 bp oligos contained the restriction sites CACC
190 and AAAC at the 5'end of the sense and antisense oligos, respectively, as described in [38].
191 Annealed oligos were cloned into the PX458 vector (Addgene plasmid #48138) digested
192 with the *BpiI* restriction enzyme (Thermo Fisher Scientific) generating the PX458-
193 PIMREG-KO vectors (KO-1, KO-2, KO-3 and KO-4). The target sequences are as follows:
194 sgRNA-1 - sense: GAGAGATCTCCGGCGCACGG and antisense:

195 CCGTGCGCCGGAGATCTCTC; sgRNA-2 - sense: CTTCTCGGTGGCAGAACATG
196 and antisense: CATGTTCTGCCACCGAGAAG; sgRNA-3 - sense:
197 CCATCAGGAGACCTCTGTAG and antisense: CTACAGAGGTCTCCTGATGG;
198 sgRNA-4 - sense: TCAACCTCAACCTCCGCGCA and antisense:
199 TGCGCGGAGGTTGAGGTTGA.

200 **2.5. Generation of CRISPR/Cas9 edited monoclonal cell lines**

201 The GBM T98G cells and the reporter cell lines HeLa EJ5-GFP and U2OS DR-GFP were
202 edited to generate PIMREG knockout cell lines (PIMREG KO-1, KO-2, KO-3, KO-4). 2 -
203 3 x 10^5 cells were seeded at 6-well plates and transfected with 2.5 µg of PX458-PIMREG-
204 KO vectors and Lipofectamine 2000 according to manufacturer's instructions
205 (ThermoFisher). Efficiently transfected cells were single sorted by Fluorescence-Activated
206 Cell Sorting (FACS) based on GFP expression. The individual cells were cultured in 96
207 well plates for clonal expansion and generation of the monoclonal cell lines. PIMREG KOs
208 were confirmed by Western blot analysis and genomic sequencing of the edited *PIMREG*
209 locus.

210 The presence of phenotypic variability among the different PIMREG KO clones, is a
211 common limitation inherent to studies relying on single-cell CRISPR/Cas9-generated KOs.
212 Particularly intriguing, was the unexpected re-expression of PIMREG protein after
213 extended culture of the GBM T98G PIMREG KO-2 cell line. This finding prompted us to
214 routinely verify PIMREG absence by immunofluorescence in all KO cell lines throughout
215 the course of the experiments. Importantly, the PIMREG KO-2 cell line that recovered
216 PIMREG protein expression (KO-2 recPIMREG) was subsequently used as a control in
217 experiments analyzing γH2AX fluorescence intensity in PIMREG KO and WT cells
218 following IR exposure.

219

220 **2.6. Cell cycle analysis**

221 1 x 10^6 cells were fixed in 70 % ethanol for 30 min on ice, washed with PBS, treated with
222 RNAse A solution (100 µg/ml) and stained with 100 µg/ml propidium iodide (PI). Cell
223 cycle analysis was performed using FACS Symphony A1 (BD Biosciences) and FlowJo
224 software version 10. Statistical analyses were performed with Two-way ANOVA, using
225 GraphPad Prism 9.

226 **2.7. Cell viability analysis**

227 Cell viability was assessed with either Annexin V or Zombie NIR staining. For the Annexin
228 V staining, cells were washed with the Annexin V Binding Buffer (BD Pharmingen™) and
229 incubated with 5 µl Annexin V reagent (BD Pharmingen™) for 15 min at RT followed by
230 2.5 µL of PI solution (Miltenyi Biotec) (100 µg/mL). For the Zombie NIR staining, cells
231 were incubated with Zombie NIR reagent (BioLegend) (1:400) for 15 min, washed with
232 PBS, fixed with 2 % paraformaldehyde (PFA) for 15 min and resuspended in 1 %
233 glycine/PBS. Cell viability was analyzed using FACS Symphony A1 (BD Biosciences) and
234 FlowJo software version 10.

235 **2.8. Immunoblotting and Immunoprecipitation**

236 Cells were lysed in lysis buffer with protease inhibitors (10 mM EDTA, 100 mM Tris-HCl
237 pH 7.5; 1 % Triton X-100, 10 mM Sodium Pyrophosphate ($Na_2P_2O_7$), 100 mM Sodium
238 Fluoride (NaF), 10 mM Sodium Orthovanadate (Na_3VO_4); 2 mM PMSF). Protein extracts
239 were separated by electrophoresis on 12 % or on a gradient 2.5-12.5 % SDS polyacrylamide
240 (SDS-PAGE) gel and transferred to a nitrocellulose membrane (GE Healthcare Life
241 Science). Membranes were blocked with 1 % BSA or 5 % low fat milk and probed with a
242 specific antibody, followed by incubation with a secondary antibody conjugated to
243 horseradish peroxidase (HRP). Protein signals were detected by chemiluminescence and
244 the images were captured by ChemiDoc™ Imaging System (Bio-Rad). Primary antibodies

245 were: anti-PIMREG (anti-CATS 2C4) (1:10) (Archangelo et al., 2008), anti-β-Actin
246 (ThermoFisher Scientific, # AM4302 and Santa Cruz Biotechnology sc-1616) (1:10000
247 and 1:2000, respectively), anti-α-tubulin (Santa Cruz Biotechnology sc-5286) (1:1000),
248 anti-phospho-H2AX (S139) (Cell Signaling Technology, #2577 and #80312) (1:500 and
249 1:1000, respectively), anti-phospho-ATM (S1981) (Sigma-Aldrich, clone 10H11.E12)
250 (1:1000), anti-ATM (Sigma-Aldrich, clone MAT3-4G10/8) (1:1000), anti-phospho-DNA-
251 PKcs (S2056) (Cell Signaling Technology, #68716) (1:1000), anti-DNA-PKcs (Cell
252 Signaling Technology, #38168) (1:1000), anti-phospho-CHK1 (S345) (Cell Signaling
253 Technology, #2348) (1:1000), anti-CHK1 (Cell Signaling Technology, #2360) (1:1000),
254 anti-phospho-KAP1 (S824) (Abcam, ab243870) (1:1000), anti-KAP1 (Abcam, ab109545)
255 (1:1000) and anti-phospho-ATM/ATR substrate (Phospho-(Ser/Thr) ATM/ATR Substrate;
256 Cell Signaling Technology, #2851) (1:1000). The secondary antibodies were anti-mouse
257 (Santa Cruz Biotechnology, sc-2064) (1:3000), anti-rat (KPL, 52200364) (1:3000), anti-
258 goat (Santa Cruz Biotechnology, sc-2354) (1:3000) and anti-rabbit (Abcam, ab6721)
259 (1:3000). The blots were stripped with Restore Western Blot Stripping Buffer (Thermo
260 Scientific, YE366939) before reprobing. Quantitative analyses of the optical intensities of
261 the protein bands were determined with UN-SCAN-IT gel 6.1 software (Silk Scientific Inc.,
262 UT) and normalized by control protein.
263 For immunoprecipitation, 170 - 290 µg of cellular extracts were incubated overnight with
264 50 µl of monoclonal rat anti-PIMREG (anti-CATS 2C4), 1:20 (v/v) rabbit anti-phospho-
265 ATM/ATR substrate antibodies and respective isotype controls (1.6 µg of rat IgG Santa
266 Cruz Biotechnology, sc-2026 and 21 µg of rabbit IgG, Jackson ImmunoResearch
267 Laboratories, Inc., 011-000-003) at 4 ºC, under rotation. The next day, 40 µl of Protein G-
268 Agarose (Roche) was added and incubated further for 3 h. Beads were extensively washed
269 with lysis buffer (50 mM Tris-HCl pH 8, 150 mM NaCl, 0.1 % SDS, 1 % IGEPAL, and 0.5

270 % sodium deoxycholate), resuspended in SDS sample buffer, boiled, and separated on a 12
271 % SDS-PAGE gel. Subsequent Western blot analysis was carried out with the antibodies
272 anti-PIMREG (anti-CATS 2C4) and anti-phospho-ATM/ATR substrate.

273 **2.9. Immunofluorescence**

274 Cells grown on coverslips were treated with TMZ and IR, fixed and permeabilized by
275 sequential incubation in 1 % PFA/ 0.5 % Triton X-100 followed by 1 % PFA/ 0.3 % Triton
276 X-100 and 0.5 % methanol for 20 min and blocked for 1 h with blocking solution (0.5 %
277 Triton X-100, 1 mM EDTA, 1 mg/mL BSA, and 0.03 % FBS) at RT. Coverslips were
278 incubated for 1 h with the primary antibodies diluted in blocking solution: anti-PIMREG
279 (Anti-CATS-2C4) (1:10) and anti-phospho-H2AX (S139) (Cell Signaling Technology,
280 #80312) (1:100). Secondary Alexa Fluor-conjugated antibodies Alexa Fluor anti-rat 488
281 (Invitrogen, A-11006) (1:500), Alexa Fluor anti-mouse 555 (Invitrogen, A21325) (1:600)
282 and Alexa Fluor anti-rabbit 594 (Thermo Fisher Scientific, A32754) (1:600) were used for
283 detection of the primary antibodies. Nuclei were counterstained with 300 nM DAPI solution
284 and coverslips were mounted on slides using Fluoromount-G™ Mounting Medium
285 (Invitrogen).

286 Images were acquired using a Leica SP5 confocal microscope and a Leica CTR 6000
287 Fluorescence Microscope equipped with LAS AF software, employing 100x magnification
288 in z-stack mode. γH2AX fluorescence intensity was quantified using ImageJ Fiji software
289 (version 2.14). Corrected Total Cell Fluorescence (CTCF) was calculated for each nucleus
290 (CTCF = IntDen - (mean background × area)). A minimum of 75 cells were analysed per
291 condition per experiment.

292 For colocalization, line scan analysis was performed using the "plot profile" tool in ImageJ
293 Fiji (version 2.14). Fluorescence intensity values (gray values) across distance (µm) for
294 each channel were plotted as line graphs in GraphPad Prism 9.

295 **2.10. DNA repair assay**

296 The frequency of HR and NHEJ were estimated using U2OS DR-GFP and HeLa EJ5-GFP
297 reporter cells [39,40]. 3 x 10^5 HeLa EJ5-GFP and 1 x 10^5 U2OS DR-GFP cells WT and
298 PIMREG KOs (KO-1, -2, -3 and -4) were seeded at 6-well plates and transfected with 2.5
299 µL of the *I-SceI* endonuclease expressing plasmid, which creates the DSBs (pCBASceI;
300 Addgene Plasmid #26477). Cells were collected 48 h after transfection and the percentage
301 of GFP-positive cells was determined by flow cytometry using FACS Symphony A1 or
302 Accuri C6 (BD Biosciences) and FlowJo software. Dead cells were excluded from the
303 analysis using Zombie NIR (BioLegend) staining at proportion 1:400. Fifty thousand events
304 were acquired. The percentage of GFP-positive cells of each sample was normalized by the
305 mean value of WT GFP-positive cells used as internal control for each experiment.

306 **2.11. Mass spectrometry analysis**

307 PIMREG was immunoprecipitated from cellular extracts of U87MG (900 µg) and T98G
308 (500 µg) cells treated with TMZ and DMSO using the anti-PIMREG (anti-CAST2C4)
309 antibody and protein G magnetics beads (PureProteome™ Protein G Magnetic Beads,
310 Merck). Normal rat IgG antibody (Santa Cruz Biotechnology) was used as isotype control.
311 The experiments were performed in triplicates (Supplementary Fig. S1).

312 Immunoprecipitated proteins were reduced with 10 mM dithiothreitol (DTT) at 37 °C for
313 45 min, then alkylated with 55 mM chloroacetamide at RT for 30 min in the dark. Samples
314 were mixed with NuPAGE LDS sample buffer (Thermo Fisher Scientific), incubated at
315 70 °C for 10 min, and loaded onto a NuPAGE Bis-Tris gel by electrophoresis at 200 V for
316 5 min, allowing proteins to migrate approximately 1 cm into the gel. Gels were fixed in 2
317 % acetic acid and 40 % methanol and stained with Coomassie blue. Gel bands were excised,
318 transferred to a 96-well plate, and destained with 50 mM triethylammonium bicarbonate
319 (TEAB) in 50 % ethanol for 2 h at RT followed by 1 h at 55 °C. Gel pieces were dehydrated

320 with 100 % ethanol for 10 min, rehydrated in 5 mM TEAB for 20 min, and dehydrated again
321 with 100 % ethanol for 10 min.
322 For digestion, 20 µl of trypsin solution (10 ng/µl in 5 mM TEAB) was added to each gel
323 piece and incubated at 4 °C for 15 min. Excess of trypsin solution was removed and
324 replaced with 20 µl of 5 mM TEAB, and digestion was performed overnight at 37 °C.
325 Peptides were extracted by sequential incubations: two rounds with 20 µl of 1 % formic
326 acid (FA) for 30 min each, followed by extraction with 20 µl of 60 % acetonitrile (ACN)
327 containing 0.1 % FA for 30 min. Extracted peptides were dried and stored at -20 °C until
328 LC-MS analysis.
329 Peptides were analyzed using an Orbitrap Fusion Lumos mass spectrometer (Thermo Fisher
330 Scientific) coupled to a Dionex UltiMate 3000 RSLCnano system (Thermo Fisher
331 Scientific). Peptide separation was performed at a flow rate of 300 nL/min on a 50-min
332 linear gradient from 4% to 32% solvent B (0.1 % FA and 5 % DMSO in ACN) in solvent
333 A (0.1 % FA and 5 % DMSO in water). The MS was operated in positive ion mode using
334 data-dependent acquisition (Top20 method). Full MS scans (MS1) were acquired in the
335 Orbitrap from 360 to 1300 m/z at a resolution of 60,000 in profile mode, with an automatic
336 gain control (AGC) target of 4e5 and a maximum injection time (maxIT) of 50 ms. For
337 MS/MS (MS2) acquisition, precursor ions were isolated with a 1.7 Th window, fragmented
338 by higher-energy collisional dissociation (HCD) at a normalized collision energy (NCE) of
339 30 %, and analyzed in the Orbitrap at a resolution of 30,000 in centroid mode (AGC target
340 of 2e5 and maxIT of 50 ms). Dynamic exclusion was set to 20 s.
341 MS raw files were processed using MaxQuant (version 1.6.17.0) and searched against the
342 UniProtKB human reference proteome (downloaded on 2019-07-15) with default
343 parameters. Carbamidomethylation of cysteine was set as a fixed modification, and
344 oxidation of methionine as well as N-terminal protein acetylation were defined as variable

345 modifications. Protein groups labeled as "reverse" or "potential contaminant" were
346 excluded. Protein abundance was estimated based on iBAQ values, and missing values were
347 imputed with a constant value corresponding to a log2 iBAQ intensity of 10 to enable
348 downstream statistical analysis. Differential expression analysis was performed using a
349 two-sample t-test, and p-values were adjusted for multiple testing using the Benjamini-
350 Hochberg procedure.
351 The comparison between PIMREG immunoprecipitates vs. IgG under vehicle (DMSO)
352 conditions (PIMREG IP vs. IgG) identified the PIMREG-interacting partners (i.e.
353 significantly upregulated proteins), considered as the *bona fide* PIMREG interactome. The
354 comparison between PIMREG immunoprecipitates from TMZ vs. vehicle (TMZ vs.
355 DMSO) revealed TMZ-induced alterations in PIMREG interactions and gave rise to the
356 TMZ-regulated interactome. The identified proteins were filtered by significance based on
357 $\log_2$ fold change cutoff > 1 (PIMREG IP vs. IgG) and $\log_2$ fold change cutoff > 1 and < -1
358 (TMZ vs. DMSO) and adjusted p-value < 0.05. Data was analyzed using R software
359 (version 4.3.2) and Excel (Microsoft Office).
360 Upregulated proteins in the TMZ-regulated interactome are proteins that interact with
361 PIMREG only under TMZ treatment or show increased association under treatment
362 whereas the downregulated proteins are those with reduced or lost binding upon TMZ
363 treatment.

364 **2.12. Gene Ontology and network analyses**

365 Gene Ontology (GO) analysis was carried out using the EnrichR platform
366 (https://maayanlab.cloud/Enrichr/). Terms with adjusted p-value < 0.05 were considered
367 statistically significant.
368 PIMREG and its interacting proteins were searched for interaction networks using the
369 STRING database (https://string-db.org). Interactions determined experimentally,

370 registered in curated databases, extracted from text mining or coexpression data were
371 considered, using a medium confidence (0.400) interaction score. Network was clustered
372 using the MCL clustering algorithm, with an inflation parameter of 3.
373

374 **3. Results**

375 **3.1. GSEA analysis implicates *PIMREG* in DNA repair and splicing**

376 *PIMREG* expression correlates with genes associated with cell cycle, DNA replication and
377 DNA repair in GBM [35]. To dissect the relationship between high *PIMREG* expression and
378 GBM further, we performed a GSEA analysis testing for functionally enriched pathways that
379 correlate with high expression of *PIMREG* in GBM patient samples (TCGA, PanCancer
380 Atlas, 592 samples). Our analysis revealed 392 enriched gene sets related to high *PIMREG*
381 expression using the HALLMARK (17 gene sets), KEGG (65 gene sets) and REACTOME
382 (310 data sets) databases (Supplementary Table 1). In support of previous results [35], our
383 analysis uncovered correlations between high *PIMREG* expression and the gene sets from
384 several DNA repair pathways (33 out of 392 gene sets), including base excision repair (BER),
385 nucleotide excision repair (NER), mismatch repair (MMR), double-strand break repair (DSB
386 repair), homology directed repair (HDR), Fanconi anemia (FA), and UV-response (Fig. 1A,
387 Supplementary Table 2), indicating putative functions for PIMREG across multiple DNA
388 repair pathways in GBM.
389 Moreover, gene sets pertaining to RNA metabolism, such as spliceosome, RNA
390 polymerase, RNA transport, RNA degradation, processing of capped intron-containing pre-
391 mRNA and mRNA splicing were also abundant, accounting for 12.5 % of all gene sets (49
392 out of 392), suggesting an unforeseen function for *PIMREG* in RNA splicing and
393 processing (Fig. 1B, Supplementary Table 3).
394 In line with putative functions for PIMREG in DDR, we performed a correlation analysis
395 using data from the GBM patient samples uncovering a strong positive correlation between
396 *PIMREG* transcript abundance and the abundance of transcripts from essential genes
397 required for DSBs recognition and repair, including *H2AX*, *RAD51*, *RAD51AP1*, and
398 *FANCD2* (Fig. 1C).

399 Since the methylation status of the *MGMT* promoter is a well-established predictive
400 biomarker for response to TMZ treatment in gliomas [41], *PIMREG* expression was
401 additionally assessed in glioma patient samples stratified by the methylation status of the
402 *MGMT* promoter. The analysis revealed that samples with unmethylated *MGMT* promoters,
403 (MGMT proficient) possessed significantly higher levels of *PIMREG* expression compared
404 to samples with methylated *MGMT* promoters (Fig. 1D), suggesting that PIMREG is more
405 abundant in the group of patients with lower response to TMZ.
406 Altogether, these findings support our previous analyses, suggesting wide roles for
407 PIMREG during the DDR but also in RNA metabolism in GBM.

408 **3.2. PIMREG interactome in response to TMZ treatment**

409 We have previously shown that treating GBM cells with TMZ triggers an increase in
410 PIMREG protein levels, as cells accumulate DNA lesions. We hypothesized that PIMREG
411 accumulation is required to mitigate DNA lesions induced by TMZ treatment [35].
412 To gain insight into the functional implications of PIMREG accumulation in response to
413 TMZ treatment, PIMREG was immunoprecipitated from GBM cells treated with TMZ and
414 its interactome identified by mass spectrometry (Supplementary Fig. S1).
415 To ensure reproducibility, only the proteins with peptides detected in all three replicates and
416 filtered by significance based on $\log_2$ fold change cutoff > 1 (PIMREG IP vs. IgG) or $\log_2$
417 fold change cutoff > 1 and < -1 (TMZ vs. DMSO) and adjusted p-value < 0.05, were
418 considered and identified as PIMREG interactors.
419 In U87MG cells, a total of 36 proteins were identified as PIMREG interacting partners (Fig.
420 2A and Supplementary Table 4), whereas 29 proteins were identified as TMZ-regulated
421 PIMREG interactors (Fig. 2B and Supplementary Table 5). In T98G cells, 8 proteins were
422 identified as PIMREG interacting partners (Fig. 2C and Supplementary Table 6) while 4 were
423 identified as TMZ-induced interacting proteins (Fig. 2D and Supplementary Table 7).

424 To better understand the molecular functions of PIMREG, we analyzed its protein interaction
425 network using the STRING database. Both upregulated and downregulated interacting
426 proteins were used for this analysis. This approach strongly implicated PIMREG in splicing
427 and ribosome biology, as protein clusters related to these functions were identified in both
428 PIMREG interactome and TMZ-regulated interactome of U87MG cells, albeit with distinct
429 sets of interactors. Additionally, a cluster of proteins related to NADH dehydrogenase
430 activity and one unidentified cluster of PIMREG and TRIP13 were observed in the TMZ-
431 regulated interactome only, whereas a cluster related to immunoglobulin complex was
432 observed in the PIMREG interactome only (Fig. 2E and 2F). For the T98G cells, a cluster of
433 proteins related to the Polycomb complex was observed within the TMZ-regulated PIMREG
434 interactors (Fig. 2G), whilst no cluster was formed among the proteins identified in the
435 PIMREG interactome.
436 GO analysis of the proteins identified as the TMZ-regulated interactors of PIMREG in
437 U87MG retrieved 10 ontological annotations whereas the proteins identified in PIMREG
438 interactome and TMZ-regulated interactome of T98G, retrieved 16 and 50, respectively.
439 These ontological annotations were classified according to their related biological processes
440 (BP) (Fig. 2H, 2I and 2J; Supplementary Tables 8, 9 and 10). The BP terms obtained for
441 TMZ-regulated PIMREG interacting proteins in U87MG cells were related to RNA
442 splicing/processing, cell division/proliferation and mitochondrial metabolism (Fig. 2H;
443 Supplementary Table 8). The BP terms obtained for PIMREG interactome in T98G cells were
444 related to insulin pathway, transcription/mRNA processing, immune response, protein
445 transport, and cell signaling (Fig. 2I; Supplementary Table 9). Lastly, the BP terms described
446 for TMZ-regulated PIMREG interacting proteins identified in the T98G cells were related to
447 cell differentiation/development, transcription/translation, macromolecule metabolic process,
448 telomere maintenance, IFN signaling, ribosome biogenesis, apoptosis, DNA replication and

449 cell division. Notably, the BP related to DDR exhibited the highest number of ontological
450 annotations, which included telomere maintenance- (GO:1904507), intrinsic apoptotic-
451 (GO:0008630), mitotic check-point (GO:0044773) signaling pathways in responses to DNA
452 damage as well as regulation of DNA repair (GO:0006282) and DSB repair via homologous
453 recombination (GO:0000724), underscoring the role of PIMREG in the DDR of T98G cells
454 treated with TMZ (Fig. 2J; Supplementary Table 10).

455 **3.3. PIMREG is a substrate of ATM/ATR in GBM cells treated with TMZ**

456 PIMREG is a phospho-protein [42] containing residues, which lie within the S/TQ motif, a
457 known target site for ATM and ATR phosphorylation [43]. To ask if PIMREG is a substrate
458 of ATR/ATM, we precipitated endogenous PIMREG from TMZ- and DMSO-treated as well
459 as untreated T98G GBM cells and blotted the precipitated protein against the phospho-
460 ATM/ATR substrate antibody (Fig. 3A) used to detect proteins containing the phosphorylated
461 substrate motif of ATM/ATR. Under all conditions we identified the precipitated PIMREG
462 protein (Fig. 3A, lower panel, lanes 3, 6 and 9). In the reciprocal immunoprecipitation
463 experiment, precipitated phospho-ATM/ATR substrates (Fig. 3B, upper panel) were blotted
464 against anti-PIMREG antibody (Fig. 3B, lower panel) and the PIMREG protein could be
465 detected by anti-PIMREG among the precipitated phospho-ATM/ATR substrates in TMZ-
466 treated cells (Fig. 3B, lower panel, lane 9). These results strongly suggest that PIMREG is a
467 direct substrate for ATM/ATR kinases *in vivo.*

468 **3.4. PIMREG deletion interferes with γH2AX accumulation in GBM cells**

469 To investigate the role of PIMREG in the cellular response to DNA damage, we generated
470 PIMREG knockout GBM T98G cell lines (PIMREG KO-1, KO-2, KO-3 and KO-4) and
471 measured γH2AX levels by Western blot to monitor DNA damage and signaling.
472 Quantification of γH2AX band intensity revealed that PIMREG KOs exhibited higher levels

473 of γH2AX than the wild-type (WT) cells (Fig. 4A and 4B; Supplementary Fig. 2A),
474 suggestive of higher basal DNA damage levels and/or genomic instability in the absence of
475 PIMREG when compared to controls.
476 We next examined the relative amount of DNA damage in the PIMREG KOs treated with
477 TMZ and IR to control cells. As expected, γH2AX signal increased in WT cells treated with
478 both TMZ and IR compared to DMSO or non-irradiated (NI) control cells (Fig. 4C and 4E,
479 middle panels).
480 Although PIMREG KOs exhibit higher levels of basal γH2AX than WT cells, when the
481 amount of γH2AX of TMZ- or IR-treated cells was normalized by those of DMSO or NI
482 (TMZ/DMSO or IR/NI), comparable levels of γH2AX accumulation were observed in
483 PIMREG KOs and WT treated with TMZ, with the exception of PIMREG KO-4 which
484 exhibited reduced levels of γH2AX accumulation (Fig. 4D; Supplementary Fig. 2B).
485 In PIMREG KOs cells treated with IR, reduced levels of γH2AX accumulation were
486 observed across all clones (Fig. 4F; Supplementary Fig. 2C). Taken together, these results
487 suggest that although PIMREG KO cells exhibit high levels of basal γH2AX, its absence
488 compromises the accumulation of γH2AX induced following exposure to genotoxic stress.
489 To complement these results, immunofluorescence experiments were performed to
490 examine the fluorescence intensity of γH2AX in the nuclei of PIMREG KO and WT GBM
491 cells treated with TMZ or exposed to IR. As shown in Figure 5, TMZ and IR treatments
492 enhanced γH2AX signal in both PIMREG KOs and WT cells, compared to DMSO or non-
493 irradiated (NI) control cells. However, the overall amount of γH2AX fluorescence intensity
494 appeared significantly lower in the PIMREG KOs compared to WT cells (Fig. 5), with the
495 exception of PIMREG KO-3 exposed to IR which exhibited similar levels of γH2AX
496 accumulation compared to WT. Interestingly, in one PIMREG KO cell line (KO-2), where
497 PIMREG protein expression was unexpectedly restored (KO-2-recPIMREG) (Fig. 5C and

498 5E), IR exposure led to the opposite effect, with markedly increased γH2AX accumulation
499 (Fig. 5D). At present we do not know the underlying mechanism of PIMREG recovery.
500 Nevertheless, the data suggest that the presence of PIMREG could rescue the impaired
501 DNA damage response phenotype observed in its absence, which is supported by the fact
502 that the same KO-2 cell line, prior to recovery of PIMREG (Fig. 5A), exhibited significant
503 reduction of γH2AX following TMZ treatment (Fig. 5B).
504 Taken together, our results demonstrate that PIMREG deletion impairs γH2AX signaling
505 in GBM cells under conditions of genotoxic stress.

506 **3.5. PIMREG deletion compromises DNA damage signaling**

507 We next asked whether PIMREG KO affects the activation of additional DNA
508 damage response signaling molecules following treatment with to TMZ or IR (Fig. 6;
509 Supplementary Fig. S3). Besides ATM, we analyzed molecules representing different steps
510 of the DNA damage signaling cascade. These include KAP1, which facilitate DSB repair
511 in both euchromatin and heterochromatin [44]; CHK1, a critical cell-cycle checkpoint
512 regulator; and DNA-PKc, a central component of DSB signaling pathway that orchestrates
513 NHEJ-mediated repair [45]

514 Western blot analysis and quantification of phosphorylated protein band intensities
515 revealed no differences in the activation of KAP1, CHK1 or DNA-PKc between PIMREG
516 KOs and WT cells after exposure to TMZ (Fig. 6A-6F). In contrast, PIMREG KO cells
517 exposed to IR showed a consistent trend of reduced ATM, KAP1 and CHK1 activation
518 compared to WT cells. This reduction was most evident at 0.5 h post-irradiation (Fig. 6G-
519 6L). Activation of DNA-PKc was unaffected in PIMREG KOs cells relative to WT
520 following IR exposure (Fig. 6M and 6N). Thus, loss of PIMREG alters DDR signaling in
521 irradiated GBM cells.

522 **3.6. PIMREG deletion interferes with the repair of DSBs**

523 ATM and γH2AX are key regulators of DSBs signaling cascade to promote repair [45,46].
524 Given ATM/ATR can phosphorylate PIMREG and that its deletion reduces both γH2AX and,
525 putatively, may alter wider DDR signaling, we sought to investigate the impact of PIMREG
526 deletion on DSB repair.

527 To this end, we performed DNA repair assays using HR (U2OS DR-GFP) and NHEJ (HeLa
528 EJ5-GFP) reporter cell lines [39,40] in which PIMREG was deleted. In the DR-GFP and EJ5-
529 GFP reporter systems, the expression of GFP protein is restored upon HR and NHEJ repair,
530 respectively.

531 The absence of PIMREG significantly impaired DNA repair by HR in the U2OS DR-GFP
532 PIMREG KOs (KO-1, KO-2, KO-3 and KO-4). Although the reduction of the HR-mediated
533 repair was not statistically significant in the PIMREG KO-2 cell line, this trend was
534 consistently observed across the three independent experiments (Fig. 7A). Additionally, the
535 absence of PIMREG was associated with an increase in DNA repair by the NHEJ pathway in
536 one out of four HeLa EJ5-GFP PIMREG KOs (KO-4), with a similar trend being observed in
537 the PIMREG KO-3 cell line (Fig. 7B). Together, these findings suggest that PIMREG plays
538 a role in promoting HR-mediated DSBs repair, while its absence may favor repair by NHEJ
539 pathway.

540

541

542 **4. Discussion**

543 This study greatly expands our understanding of PIMREG, redefining it from a
544 proliferation marker to an integrated component of the DDR in GBM. Our findings reveal
545 that PIMREG functions as a direct substrate for ATM/ATR kinases, interacts with key DNA
546 repair proteins, and actively facilitates the cellular response to chemotherapy- and
547 radiotherapy-induced DNA damage. By demonstrating its role in signaling and repairing of
548 DSBs, we consolidate PIMREG as a key player in maintaining genomic integrity and
549 possibly, promoting treatment resistance.

550 Pathway enrichment analysis performed using GBM patient samples revealed
551 putative functions for PIMREG across multiple DNA repair pathways and in RNA splicing
552 and processing, finding supported by our mass spectrometry data. Specifically, we
553 uncovered in our PIMREG interactome associations with key DNA repair factors involved
554 in HR-mediated resolution of DSB, including YY1 in T98G cells, and TRIP13 and PRMT5
555 in U87MG.

556 YY1 is a transcription factor, which complex with chromatin-remodeling factors
557 and is essential for HR-based DNA repair [47]. TRIP13 is an ATPase involved in early
558 DNA damage sensing and ATM signal amplification [48] thereby contributing to the
559 promotion of HR [49]. PRMT5, an arginine methyltransferase with described roles in
560 splicing and stemness in GBM [50] is also a key regulator of HR-mediated DSB repair [51].
561 Notably, such associations between PIMREG and DDR-related proteins were only
562 observed in TMZ-regulated interactomes, suggesting that these interactions or the
563 modulation of binding of these proteins to PIMREG are specific to TMZ exposure, and thus
564 DNA damage, further evidencing roles for PIMREG in DSB repair by HR.

565 In both TMZ-regulated PIMREG interactome and PIMREG interactome under
566 control conditions, we identified putative interactions between PIMREG and proteins

567 related to RNA splicing and processing. To the best of our knowledge, this is the first report
568 linking PIMREG to RNA metabolism. Such observations provide a strong foundation for
569 future investigation into PIMREG's role in RNA metabolism in GBM. Moreover, the
570 difference in the splicing network observed between PIMREG interactome under control
571 condition or induced by TMZ treatment evidences a dynamic role in RNA processing that
572 may be influenced in response to the genotoxic stress. It is tempting to speculate that this
573 shift in the splicing network relates to a non-canonical function of PIMREG in DDR-
574 specific splicing. Mounting evidence supports crosstalk between RNA splicing and the
575 DDR [52–57], for example, the splicing factor SF3B2, a putative interactor of PIMREG
576 identified in this study, has been previously linked to HR-mediated repair of DSB [58]. In
577 support, we have recently reported UHMK1, a known PIMREG interacting protein [42], as
578 a splicing regulatory kinase [59]. In addition to phosphorylating PIMREG and several
579 mRNA related proteins, UHMK1 also regulates the phosphorylation of critical DDR
580 proteins, including RAD54L [60], THRAP3, BCLAF1 [61], and TPT1 [62].

581 Another PIMREG-associated function observed from TMZ-regulated PIMREG
582 interactome was related to NADH dehydrogenase activity and mitochondrial metabolism,
583 suggestive of a potential role for PIMREG in mitochondrial regulation under genotoxic
584 stress. Though metabolic reprogramming is a known mechanism of TMZ resistance in
585 GBM [63], how PIMREG contributes in this context remains to be investigated.

586 We observed distinct PIMREG protein interacting profiles between the two GBM
587 cell lines. Though both cell lines support TMZ-induced PIMREG interactions with DDR-
588 related proteins, interactions related to RNA splicing and mitochondrial metabolism
589 appeared exclusive to U87MG cells. Such differences likely reflect the distinct genetic
590 background of the two cell lines: T98G cells are MGMT-proficient and carry *TP53*

591 mutation, while U87MG cells are MGMT-deficient and *TP53* wild-type, features that
592 enable distinct response to TMZ treatment [64].

593 Surprisingly, several proteins previously reported to interact with PIMREG were
594 not identified in our dataset, including PICALM [65], UHMK1 [42], PrPC [66], ROD1
595 [67], NuRD complex [14], STAT3 [17], NFkB/p65 [20], and BRSK2 [25]. A plausible
596 explanation is that these interactions were originally identified in different cell lines.

597 In summary, our proteomic findings expand the current understanding of
598 PIMREG's interaction network in established and novel cellular processes under both
599 physiological and genotoxic stress contexts of GBM cells.

600 PIMREG has two amino acid residues, serine at position 137 (S137) and threonine
601 at position 114 (T114) that could be sites for ATM/ATR phosphorylation [43]. Our data
602 shows that PIMREG is recognized by the phospho-ATM/ATR substrate antibody,
603 suggestive of PIMREG as a direct substrate of these DDR kinases. This is further supported
604 by the identification of S137 and T114 of PIMREG as phosphosites in proteomic studies
605 enriched for phospho-ATM/ATR substrates and curated into PhosphoSitePlus® database
606 (http:// www.phosphosite.org). Notably, phosphorylated PIMREG was detected under
607 DMSO- and TMZ-treated, as well as in untreated conditions. Therefore, whether
608 ATM/ATR-mediated phosphorylation of PIMREG is specifically induced in response to
609 DNA damage or occurs as part of a broader mechanism remains to be determined.

610 PIMREG deficient cells in the absence of genotoxic stress exhibited elevated levels
611 of γH2AX, suggesting PIMREG importance for genomic stability. Conversely, upon
612 exposure to TMZ or IR, these cells overall exhibited an impaired γH2AX response.
613 Quantification of γH2AX fluorescence intensity confirmed reduced γH2AX in both TMZ
614 and IR treated KO cells. However, under IR treatment, in which three out of four PIMREG
615 KO cell lines were assessed, reduced levels of γH2AX were observed exclusively in one

616 PIMREG KO cell line.

617 Unexpectedly, the PIMREG KO-2 cell line restored PIMREG protein expression
618 after extended culturing. Remarkably, upon genotoxic stress, PIMREG KO-2 that regained
619 PIMREG (KO-2-recPIMREG) displayed increased levels of γH2AX, effectively reversing
620 the phenotype observed in early passages and highlighting the heterogeneity among the KO
621 cell lines. The mechanism behind PIMREG re-expression in the KO-2 cell line remains
622 unclear. However, given that the T98G cells employed for genome editing, are highly
623 polyploid cells [68], it is plausible that one or more *PIMREG* alleles would lie within
624 chromatin regions that were inaccessible to Cas9 at the time of editing. Over time, selective
625 pressures during cell culture may have led to chromatin remodeling, enabling reactivation
626 of a previously silenced, unedited allele and restoration of PIMREG expression.

627 However, this study lacks a formal rescue experiment in which PIMREG is
628 reintroduced exogenously into KO cells. Such an experiment would definitively confirm
629 that the observed phenotype is specifically due to the loss of PIMREG and not potential
630 off-target effect.

631 Reduced activation of ATM (Ser1981) in both PIMREG KO cells exposed to IR
632 and in PIMREG knockdown cells treated with TMZ [35] supports roles for PIMREG in the
633 ATM/ATR and γH2AX signaling under damage. Given γH2AX represents a key early
634 event in DSB signaling [45], PIMREG may also act during the early stages of the cell
635 response to damage. Consistent with this, we demonstrated that KAP1 activation was
636 significantly impaired in PIMREG KOs cells exposed to IR. KAP1 is a protein involved in
637 chromatin condensation. Following DSB induced by IR, ATM phosphorylates KAP-1 at
638 S824 at the site of damage, where it colocalizes with γH2AX foci and rapidly spreads
639 throughout the chromatin [69]. Phosphorylated KAP1 facilitates DSB repair in both
640 euchromatin and heterochromatin [44].

641 Importantly, we demonstrated that loss of PIMREG significantly impacts DSB
642 repair by reducing HR-mediated repair whereas NHEJ repair was only mildly enhanced in
643 two out four KO cell lines. Notably, DNA-PKc activation, a central orchestrator of NHEJ,
644 was unaffected by PIMREG absence after IR exposure, further supporting specific roles for
645 PIMREG during the signaling and/or activation of HR. Finally, PIMREG's influence on
646 HR may be partially explained by its expression pattern throughout the cell cycle. PIMREG
647 levels become elevated during S and G2, sharply declining as cells enter G1 [13]. HR is
648 predominantly active in S and G2 phases, due to the availability of a sister chromatid for
649 repair, thus this temporal expression profile may underlie PIMREG's preferential role in
650 supporting HR over NHEJ.

651 Overall, our findings support a role for PIMREG in facilitating DSB signaling and
652 repair following damage, however it is important to note that a degree of phenotypic
653 heterogeneity was observed across treatments (TMZ and IR) and amongst KO clones. The
654 origin of this variability may be a result of off-target effects or the clonal differences arising
655 during the monoclonal selection of the KOs.

656 We observed a distinct difference in the activation of the DNA signaling molecules
657 in PIMREG KO cells treated with TMZ or exposed to IR. These differences are likely
658 attributable to the nature and timing of DNA damage induced by each agent. IR rapidly
659 induces DSBs whereas TMZ primarily causes base alkylation. The formation of secondary
660 DSBs after TMZ treatment depends on one or more rounds of DNA replication with futile
661 MMR repair [9]. It is conceivable that our cells, treated with TMZ for 24h, harbor
662 significant lower levels of DSBs at the time point analyzed, perhaps explaining why western
663 blot analysis failed to detect substantial changes in DSB signaling in TMZ-treated PIMREG
664 KO cells. In contrast, by immunofluorescence analysis, we detected a reduction in γH2AX
665 intensity in TMZ-treated KO cells. Notably, γH2AX fluorescence intensity was

666 approximately 100-fold higher in IR-treated KO-1 cells compared to those treated with
667 TMZ, highlighting the stark difference in DSB burden between the two treatments. These
668 findings strongly implicate PIMREG as a DDR factor, specifically operating to support
669 HR-directed repair of DSBs in GBM cells. A key question emerging from this study is
670 whether PIMREG participates in these pathways directly or exerts its effects indirectly
671 through broader cellular processes.

672 Given such broad functionality for PIMREG, our data is more suggestive of
673 PIMREG as an indirect contributor to the DDR, either through the regulation of upstream
674 or parallel processes essential for an effective response to genotoxic stress. PIMREG's
675 multifaceted roles are therefore especially important to understand in the context of cancer.
676 Especially given the consistent overexpression of PIMREG in many, if not all, types of
677 cancer, suggesting dysregulation of PIMREG activity may promote tumor progression and
678 treatment resistance, not only in GBM but in other cancer types.

679 In conclusion, our findings provide new evidence that PIMREG plays a role in DSB
680 signaling and HR repair highlighting PIMREG as a potential contributor to therapy
681 resistance and a promising target for future cancer therapies.

682

683

684

Credit authorship contribution statement

Maria Vitória de Rizzo Gasparini: Investigation, Conceptualization, Visualization, Formal analysis, Writing - Original Draft. **Laís do Carmo:** Investigation, Visualization, Formal analysis, Writing - Original Draft. **Giovanna Gonçalves de Almeida**: Investigation, Visualization, Formal analysis, Writing - Original Draft. **Mariana Siqueira Lacerda Mamede**: Investigation. **Isabela Spido Dias**: Investigation. **Jennifer Ann Black:** Supervision, Writing - Review & Editing. **Vanessa C Arfelli:** Validation, Supervision, Writing - Review & Editing. **Yun-Chien Chang:** Investigation, Formal analysis, Writing - Review & Editing. **Stephanie Heinzlmeir:** Supervision, Writing - Review & Editing. **Bernhard Kuster:** Resources, Writing - Review & Editing. **Philipp A. Greif:** Supervision, Resources, Writing - Review & Editing. **Leticia Fröhlich Archangelo:** Conceptualization, Supervision, Writing - Original Draft, Project administration, Funding acquisition.

Declaration of competing interests

The authors declare that they have no known competing financial interests or personal relationships that could have appeared to influence the work reported in this paper.

Data availability

The raw mass spectrometry data, MaxQuant search results, and the Swiss-Prot reference database used for analysis have been deposited to the ProteomeXchange Consortium via the MassIVE partner repository with the dataset identifier PXD069394 (MassIVE ID: MSV000099465).

Supporting information

This article contains supporting information.

Acknowledgements

We thank Dr. Jeremy A. Squire for the English review and Patrícia Vianna Bonini, Camila Menezes Bonaldo (FACS) and Leandro Federiche Borges (IR) for technical assistance. Marlon Fontes Rocha and Dr. Larissa Dias da Cunha for helping with the FACS analysis. PAG acknowledges support by the Wilhelm Sander-Stiftung (Förderantrag Nr. 2014.162.3). This research was supported by the Fundação de Amparo à Pesquisa de São Paulo (FAPESP; 2019/26035-1 and 2022/08648-9 to LFA). FAPESP supports the LMMC (2004/08868-0).

References

[1] Q.T. Ostrom, M. Price, C. Neff, G. Cioffi, K.A. Waite, C. Kruchko, J.S. Barnholtz-Sloan, CBTRUS Statistical Report: Primary Brain and Other Central Nervous System Tumors Diagnosed in the United States in 2016-2020, Neuro Oncol, 25 (2023) IV1–IV99.

[2] D.N. Louis, A. Perry, P. Wesseling, D.J. Brat, I.A. Cree, D. Figarella-Branger, C. Hawkins, H.K. Ng, S.M. Pfister, G. Reifenberger, R. Soffietti, A. Von Deimling, D.W. Ellison, The 2021 WHO classification of tumors of the central nervous system: A summary, Neuro Oncol, 23 (2021) 1231–1251.

[3] Q.T. Ostrom, M.L. Shoaf, G. Cioffi, K. Waite, C. Kruchko, P.Y. Wen, D.J. Brat, J.S. Barnholtz-Sloan, J.B. Iorgulescu, National-level overall survival patterns for molecularly-defined diffuse glioma types in the United States, Neuro Oncol, 25 (2023) 799–807.

[4] R. Stupp, M.E. Hegi, W.P. Mason, M.J. van den Bent, M.J. Taphoorn, R.C. Janzer, S.K. Ludwin, A. Allgeier, B. Fisher, K. Belanger, P. Hau, A.A. Brandes, J. Gijtenbeek, C. Marosi, C.J. Vecht, K. Mokhtari, P. Wesseling, S. Villa, E. Eisenhauer, T. Gorlia, et al., Effects of radiotherapy with concomitant and adjuvant temozolomide versus radiotherapy alone on survival in glioblastoma in a randomised phase III study: 5-year analysis of the EORTC-NCIC trial, Lancet Oncol, 10 (2009) 459–466.

[5] R. Stupp, W.P. Mason, M.J. van den Bent, M. Weller, B. Fisher, M.J.B. Taphoorn, K. Belanger, A.A. Brandes, C. Marosi, U. Bogdahn, J. Curschmann, R.C. Janzer, S.K. Ludwin, T. Gorlia, A. Allgeier, D. Lacombe, J.G. Cairncross, E. Eisenhauer, R.O. Mirimanoff, Radiotherapy plus Concomitant and Adjuvant Temozolomide for Glioblastoma, New England Journal of Medicine, 352 (2005) 987–996.

[6] J.A. Nickoloff, N. Sharma, C.P. Allen, L. Taylor, S.J. Allen, A.S. Jaiswal, R. Hromas, Roles of homologous recombination in response to ionizing radiation-induced DNA damage, Int J Radiat Biol, 99 (2023) 903–914.

[7] H. Erasimus, M. Gobin, S. Niclou, E. Van Dyck, DNA repair mechanisms and their clinical impact in glioblastoma, Mutat Res Rev Mutat Res, 769 (2016) 19–35.

[8] M.E. Hegi, A.-C. Diserens, T. Gorlia, M.-F. Hamou, N. De Tribolet, M. Weller, J.M. Kros, J.A. Hainfellner, W. Mason, L. Mariani, E.C. Bromberg, P. Hau, R.O. Mirimanoff, J.G. Cairncross, R.C. Janzer, R. Stupp, MGMT Gene Silencing and Benefit from Temozolomide in Glioblastoma, 2005.

[9] W.P. Roos, B. Kaina, DNA damage-induced cell death: From specific DNA lesions to the DNA damage response and apoptosis, Cancer Lett, 332 (2013) 237–248.

[10] W.D. Wright, S.S. Shah, W.D. Heyer, Homologous recombination and the repair of DNA double-strand breaks, Journal of Biological Chemistry, 293 (2018) 10524–10535.

[11] H.H.Y. Chang, N.R. Pannunzio, N. Adachi, M.R. Lieber, Non-homologous DNA end joining and alternative pathways to double-strand break repair, Nat Rev Mol Cell Biol, 18 (2017) 495–506.

[12] D.J. Laverty, S.K. Gupta, G.A. Bradshaw, A.S. Hunter, B.L. Carlson, N.M. Calmo, J. Chen, S. Tian, J.N. Sarkaria, Z.D. Nagel, ATM inhibition exploits checkpoint defects and ATM-dependent double strand break repair in TP53-mutant glioblastoma, Nat Commun, 15 (2024).

[13] L.F. Archangelo, P.A. Greif, M. Hölzel, T. Harasim, E. Kremmer, G.K.H. Przemeck, D. Eick, A.J. Deshpande, C. Buske, M.H. de Angelis, S.T.O. Saad, S.K. Bohlander,

The CALM and CALM/AF10 interactor CATS is a marker for proliferation, Mol Oncol, 2 (2008) 356–67.

[14] W.M. Zhao, J.A. Coppinger, A. Seki, X.L. Cheng, J.R. Yates, G. Fang, RCS1, a substrate of APC/C, controls the metaphase to anaphase transition, Proc Natl Acad Sci U S A, 105 (2008) 13415–13420.

[15] I. Barbutti, J.M. Xavier-Ferrucio, J.A. Machado-Neto, L. Ricon, F. Traina, S.K. Bohlander, S.T. Olalla Saad, L.F. Archangelo, CATS (FAM64A) abnormal expression reduces clonogenicity of hematopoietic cells, Oncotarget, 7 (2016) 68385–68396.

[16] K. Hashimoto, A. Kodama, M. Ohira, M. Kimoto, R. Nakagawa, Y. Usui, Y. Ujihara, A. Hanashima, S. Mohri, Postnatal expression of cell cycle promoter Fam64a causes heart dysfunction by inhibiting cardiomyocyte differentiation through repression of Klf15, IScience, 25 (2022).

[17] Z.S. Xu, H.X. Zhang, W.W. Li, Y. Ran, T.T. Liu, M.G. Xiong, Q.L. Li, S.Y. Wang, M. Wu, H.B. Shu, H. Xia, Y.Y. Wang, FAM64A positively regulates STAT3 activity to promote Th17 differentiation and colitisassociated carcinogenesis, Proc Natl Acad Sci U S A, 116 (2019) 10447–10452.

[18] K. Hashimoto, A. Kodama, T. Honda, A. Hanashima, Y. Ujihara, T. Murayama, S.I. Nishimatsu, S. Mohri, Fam64a is a novel cell cycle promoter of hypoxic fetal cardiomyocytes in mice, Sci Rep, 7 (2017) 1–17.

[19] P. Locatelli, M.N. Belaich, A.E. López, F.D. Olea, X. Martín Uranga Vega, C.S. Giménez, J. Alejandro Simonin, M. del Rosario Bauzá, M.G. Castillo, L.A. Cuniberti, A. Crottogini, X.S. Carolina Cerrudo, X.D. Pablo Ghiringhelli, U.M. Vega, Novel insights into cardiac regeneration based on differential fetal and adult ovine heart transcriptomic analysis, Am J Physiol Heart Circ Physiol, 318 (2020) 994–1007.

[20] L. Jiang, L. Ren, X. Zhang, H. Chen, X. Chen, C. Lin, L. Wang, N. Hou, J. Pan, Z. Zhou, H. Huang, D. Huang, J. Yang, Y. Liang, J. Li, Overexpression of PIMREG promotes breast cancer aggressiveness via constitutive activation of NF-κB signaling, EBioMedicine, 43 (2019) 188–200.

[21] D. Wang, A. Hu, H. Peng, D. Li, L. Zhang, Tumor-promoting function of PIMREG in glioma by activating the β-catenin pathway, 3 Biotech, 11 (2021).

[22] J. Zhang, L. Qian, J. Wu, D. Lu, H. Yuan, W. Li, X. Ying, S. Hu, Up-regulation of FAM64A promotes epithelial-to-mesenchymal transition and enhances stemness features in breast cancer cells, Biochem Biophys Res Commun, 513 (2019) 472–478.

[23] Z. Yao, X. Zheng, S. Lu, Z. He, Y. Miao, H. Huang, X. Chu, C. Cai, F. Zou, Knockdown of FAM64A suppresses proliferation and migration of breast cancer cells, Breast Cancer, 26 (2019) 835–845.

[24] Y. Zhou, L. Ou, J. Xu, H. Yuan, J. Luo, B. Shi, X. Li, S. Yang, Y. Wang, FAM64A is an androgen receptor-regulated feedback tumor promoter in prostate cancer, Cell Death Dis, 12 (2021).

[25] K. Li, H. Lin, A. Liu, C. Qiu, Z. Rao, Z. Wang, S. Chen, X. She, S. Zhu, P. Li, L. Liu, Q. Wu, G. Wang, F. Xu, S. Li, SOD1-high fibroblasts derived exosomal miR-3960 promotes cisplatin resistance in triple-negative breast cancer by suppressing BRSK2-mediated phosphorylation of PIMREG, Cancer Lett, 590 (2024).

[26] S. Hu, H. Yuan, Z. Li, J. Zhang, J. Wu, Y. Chen, Q. Shi, W. Ren, N. Shao, X. Ying, Transcriptional response profiles of paired tumor-normal samples offer novel perspectives in pan-cancer analysis, Oncotarget, 8 (2017) 41334–41347.

[27] H. Zhu, X. Hu, Y. Ye, Z. Jian, Y. Zhong, L. Gu, X. Xiong, Pan-Cancer Analysis of PIMREG as a Biomarker for the Prognostic and Immunological Role, Front Genet, 12 (2021).
[28] C. Zhang, Y. Han, H. Huang, L. Min, L. Qu, C. Shou, Integrated analysis of expression profiling data identifies three genes in correlation with poor prognosis of triple-negative breast cancer, Int J Oncol, 45 (2014) 2025–2033.
[29] Y. Jiao, Z. Fu, Y. Li, W. Zhang, Y. Liu, Aberrant FAM64A mRNA expression is an independent predictor of poor survival in pancreatic cancer, PLoS One, 14 (2019).
[30] K. Mizuno, K. Tanigawa, N. Nohata, S. Misono, R. Okada, S. Asai, S. Moriya, T. Suetsugu, H. Inoue, N. Seki, Fam64a: A novel oncogenic target of lung adenocarcinoma regulated by both strands of mir99a (mir-99a-5p and mir-99a-3p), Cells, 9 (2020) 1–22.
[31] X. Zhao, H. Chen, Y. Qiu, L. Cui, FAM64A promotes HNSCC tumorigenesis by mediating transcriptional autoregulation of FOXM1, Int J Oral Sci, 14 (2022).
[32] H. Yao, F. Lyu, J. Ma, F. Sun, G. Tang, J. Wu, Z. Zhou, PIMREG is a prognostic biomarker involved in immune microenvironment of clear cell renal cell carcinoma and associated with the transition from G1 phase to S phase, Front Oncol, 13 (2023).
[33] W. jing Yun, L. Zhang, N. Yang, Z. guo Cui, H. mao Jiang, M. wen Ha, D. yong Yu, M. zhen Zhao, H. chuan Zheng, FAM64A aggravates proliferation, invasion, lipid droplet formation, and chemoresistance in gastric cancer: A biomarker for aggressiveness and a gene therapy target, Drug Dev Res, 84 (2023) 1537–1552.
[34] X. Wei, Y. Jiang, T. Xia, J. Du, Oncogenic role and prognostic significance of PIMREG in melanoma, Transl Cancer Res, 14 (2025) 1070–1084.
[35] R.B. Serafim, C. Cardoso, V.C. Arfelli, V. Valente, L.F. Archangelo, PIMREG expression level predicts glioblastoma patient survival and affects temozolomide resistance and DNA damage response, Biochim Biophys Acta Mol Basis Dis, 1868 (2022).
[36] Cerami et al., The cBio Cancer Genomics Portal: An Open Platform for Exploring Multidimensional Cancer Genomics Data, Cancer Discov., 2 (2012) 401–404.
[37] A. Subramanian, P. Tamayo, V.K. Mootha, S. Mukherjee, B.L. Ebert, M.A. Gillette, A. Paulovich, S.L. Pomeroy, T.R. Golub, E.S. Lander, J.P. Mesirov, Gene set enrichment analysis: A knowledge-based approach for interpreting genome-wide expression profiles, 2005.
[38] F.A. Ran, P.D. Hsu, J. Wright, V. Agarwala, D.A. Scott, F. Zhang, Genome engineering using the CRISPR-Cas9 system, Nat Protoc, 8 (2013) 2281–2308.
[39] A.J. Pierce, M. Jasin, in Mouse Embryonic Stem Cells, Molecular Toxicology Protocols. Methods in Molecular Biology, 291 (2005).
[40] N. Bennardo, A. Cheng, N. Huang, J.M. Stark, Alternative-NHEJ is a mechanistically distinct pathway of mammalian chromosome break repair, PLoS Genet, 4 (2008).
[41] W. Wick, M. Weller, M. Van Den Bent, M. Sanson, M. Weiler, A. Von Deimling, C. Plass, M. Hegi, M. Platten, G. Reifenberger, MGMT testing - The challenges for biomarker-based glioma treatment, Nat Rev Neurol, 10 (2014) 372–385.
[42] L.F. Archangelo, P.A. Greif, A. Maucuer, V. Manceau, N. Koneru, C.L. Bigarella, F. Niemann, M.T. dos Santos, J. Kobarg, S.K. Bohlander, S.T.O. Saad, The CATS (FAM64A) protein is a substrate of the Kinase Interacting Stathmin (KIS), Biochim Biophys Acta Mol Cell Res, 1833 (2013) 1269–1279.
[43] S.-T. Kim, D.-S. Lim, C.E. Canman, M.B. Kastan, Substrate Specificities and Identification of Putative Substrates of ATM Kinase Family Members*, 1999.

[44] D. White, I.U. Rafalska-Metcalf, A. V. Ivanov, A. Corsinotti, H. Peng, S.C. Lee, D. Trono, S.M. Janicki, F.J. Rauscher, The ATM substrate KAP1 controls DNA repair in heterochromatin: Regulation by HP1 proteins and serine 473/824 phosphorylation, Molecular Cancer Research, 10 (2012) 401–414.
[45] A.N. Blackford, S.P. Jackson, ATM, ATR, and DNA-PK: The Trinity at the Heart of the DNA Damage Response, Mol Cell, 66 (2017) 801–817.
[46] W.M. Bonner, C.E. Redon, J.S. Dickey, A.J. Nakamura, O.A. Sedelnikova, S. Solier, Y. Pommier, γH2AX and cancer, Nat Rev Cancer, 8 (2008) 957–967.
[47] S. Wu, Y. Shi, P. Mulligan, F. Gay, J. Landry, H. Liu, J. Lu, H.H. Qi, W. Wang, J.A. Nickoloff, C. Wu, Y. Shi, A YY1-INO80 complex regulates genomic stability through homologous recombination-based repair, Nat Struct Mol Biol, 14 (2007) 1165–1172.
[48] H. Jeong, M. Wie, I.J. Baek, G. Sohn, S.H. Um, S.G. Lee, Y. Seo, J. Ra, E.A. Lee, S. Kim, B.G. Kim, R.A. Deshpande, T.T. Paull, J.S. Han, T. Kwon, K. Myung, TRIP13 Participates in Immediate-Early Sensing of DNA Strand Breaks and ATM Signaling Amplification through MRE11, Cells, 11 (2022).
[49] C.S. Clairmont, P. Sarangi, K. Ponnienselvan, L.D. Galli, I. Csete, L. Moreau, G. Adelmant, D. Chowdhury, J.A. Marto, A.D. D'Andrea, TRIP13 regulates DNA repair pathway choice through REV7 conformational change, Nat Cell Biol, 22 (2020) 87–96.
[50] P. Sachamitr, J.C. Ho, F.E. Ciamponi, W. Ba-Alawi, F.J. Coutinho, P. Guilhamon, M.M. Kushida, F.M.G. Cavalli, L. Lee, N. Rastegar, V. Vu, M. Sánchez-Osuna, J. Coulombe-Huntington, E. Kanshin, H. Whetstone, M. Durand, P. Thibault, K. Hart, M. Mangos, J. Veyhl, et al., PRMT5 inhibition disrupts splicing and stemness in glioblastoma, Nat Commun, 12 (2021) 1–17.
[51] T.L. Clarke, M.P. Sanchez-Bailon, K. Chiang, J.J. Reynolds, J. Herrero-Ruiz, T.M. Bandeiras, P.M. Matias, S.L. Maslen, J.M. Skehel, G.S. Stewart, C.C. Davies, PRMT5-Dependent Methylation of the TIP60 Coactivator RUVBL1 Is a Key Regulator of Homologous Recombination, Mol Cell, 65 (2017) 900-916.e7.
[52] L. Shkreta, B. Chabot, The RNA splicing response to DNA damage, Biomolecules, 5 (2015) 2935–2977.
[53] S.C. Lenzken, A. Loffreda, S.M.L. Barabino, RNA splicing: A new player in the DNA damage response, Int J Cell Biol, (2013).
[54] A. Montecucco, G. Biamonti, Pre-mRNA processing factors meet the DNA damage response, Front Genet, 4 (2013).
[55] M. Tresini, D.O. Warmerdam, P. Kolovos, L. Snijder, M.G. Vrouwe, J.A.A. Demmers, W.F.J. Van Ijcken, F.G. Grosveld, R.H. Medema, J.H.J. Hoeijmakers, L.H.F. Mullenders, W. Vermeulen, J.A. Marteijn, The core spliceosome as target and effector of non-canonical ATM signalling, Nature, 523 (2015) 53–58.
[56] C. Naro, P. Bielli, V. Pagliarini, C. Sette, The interplay between DNA damage response and RNA processing: The unexpected role of splicing factors as gatekeepers of genome stability, Front Genet, 6 (2015).
[57] A.S. Bader, B.R. Hawley, A. Wilczynska, M. Bushell, The roles of RNA in DNA double-strand break repair, Br J Cancer, 122 (2020) 613–623.
[58] R. Prados-Carvajal, A. López-Saavedra, C. Cepeda-García, S. Jimeno, P. Huertas, Multiple roles of the splicing complex SF3B in DNA end resection and homologous recombination, DNA Repair (Amst), 66–67 (2018) 11–23.
[59] V.C. Arfelli, Y.-C. Chang, J.W. Bagnoli, P. Kerbs, F.E. Ciamponi, L.M. da S. Paz, S. Pankivskyi, J. de Matha Salone, A. Maucuer, K.B. Massirer, W. Enard, B. Kuster,

P.A. Greif, L.F. Archangelo, UHMK1 is a novel splicing regulatory kinase, Journal of Biological Chemistry, 299 (2023) 103041.

[60] J.M. Mason, K. Dusad, W.D. Wright, J. Grubb, B. Budke, W.D. Heyer, P.P. Connell, R.R. Weichselbaum, D.K. Bishop, RAD54 family translocases counter genotoxic effects of RAD51 in human tumor cells, Nucleic Acids Res, 43 (2015) 3180–3196.

[61] J. Vohhodina, E.M. Barros, A.L. Savage, F.G. Liberante, L. Manti, P. Bankhead, N. Cosgrove, A.F. Madden, D.P. Harkin, K.I. Savage, The RNA processing factors THRAP3 and BCLAF1 promote the DNA damage response through selective mRNA splicing and nuclear export, Nucleic Acids Res, 45 (2017) 12816–12833.

[62] J. Zhang, S.M. De Toledo, B.N. Pandey, G. Guo, D. Pain, H. Li, E.I. Azzam, Role of the translationally controlled tumor protein in DNA damage sensing and repair, Proc Natl Acad Sci U S A, 109 (2012).

[63] H.Y. Li, Y.H. Feng, C.L. Lin, T.I. Hsu, Mitochondrial Mechanisms in Temozolomide Resistance: Unraveling the Complex Interplay and Therapeutic Strategies in Glioblastoma, Mitochondrion, 75 (2024).

[64] M. Hermisson, A. Klumpp, W. Wick, J. Wischhusen, G. Nagel, W. Roos, B. Kaina, M. Weller, O6-methylguanine DNA methyltransferase and p53 status predict temozolomide sensitivity in human malignant glioma cells, J Neurochem, 96 (2006) 766–776.

[65] L.F. Archangelo, J. Gläsner, A. Krause, S.K. Bohlander, The novel CALM interactor CATS influences the subcellular localization of the leukemogenic fusion protein CALM/AF10, Oncogene, 25 (2006) 4099–4109.

[66] J. Satoh, S. Obayashi, T. Misawa, K. Sumiyoshi, K. Oosumi, H. Tabunoki, Protein microarray analysis identifies human cellular prion protein interactors, Neuropathol Appl Neurobiol, 35 (2009) 16–35.

[67] T.F. Brazão, J. Demmers, W. Van Ijcken, J. Strouboulis, M. Fornerod, L. Romão, F.G. Grosveld, A new function of ROD1 in nonsense-mediated mRNA decay, FEBS Lett, 586 (2012) 1101–1110.

[68] G.H. Stein, T98G: An anchorage-independent human tumor cell line that exhibits stationary phase G1 arrest in vitro, J Cell Physiol, 99 (1979) 43–54.

[69] Y. Ziv, D. Bielopolski, Y. Galanty, C. Lukas, Y. Taya, D.C. Schultz, J. Lukas, S. Bekker-Jensen, J. Bartek, Y. Shiloh, Chromatin relaxation in response to DNA double-strand breaks is modulated by a novel ATM-and KAP-1 dependent pathway, Nat Cell Biol, 8 (2006) 870–876.

[70] T. Aparicio, R. Baer, J. Gautier, DNA double-strand break repair pathway choice and cancer, DNA Repair (Amst), 19 (2014) 169–175.

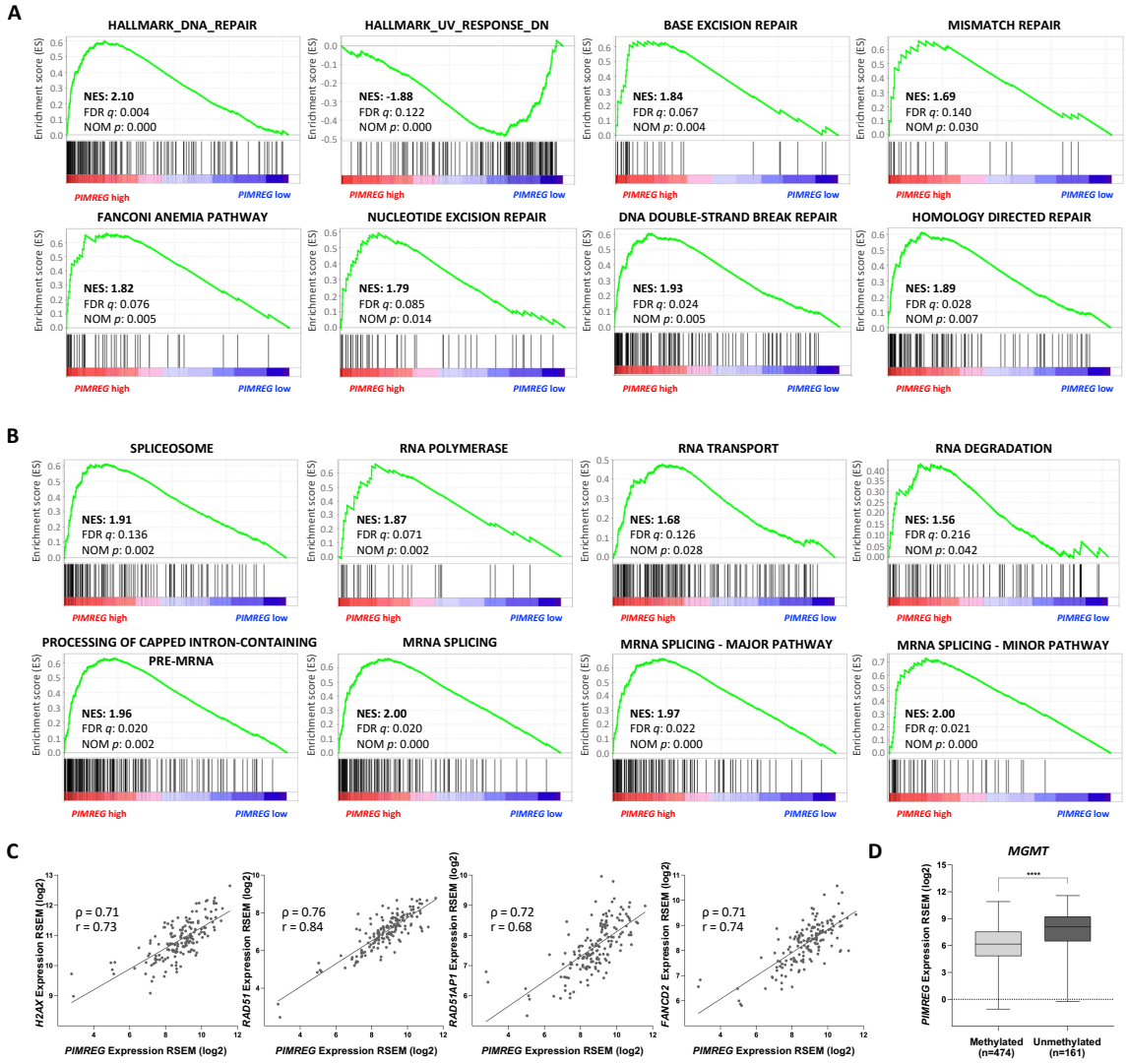

Fig. 1: GBM samples with *PIMREG* high expression are enriched for DDR and RNA metabolism. (**A**) GSEA analysis reveals enriched gene sets related to DDR and (**B**) RNA metabolism. (**C**) Correlation plot between the transcript levels of *PIMREG* and the DDR coding genes, *H2AX*, *RAD51*, *RAD51AP1* and *FANCD2* in GBM patient samples. (ρ) Spearman's correlation coefficient and (r) Pearson's correlation coefficient. (**D**) *PIMREG* expression in glioma patients classified according to methylation status of the *MGMT* promoter region. (****) *p*-value < 0.0001, Mann-Whitney two-tailed test. RSEM: RNAseq by Expectation-Maximization.

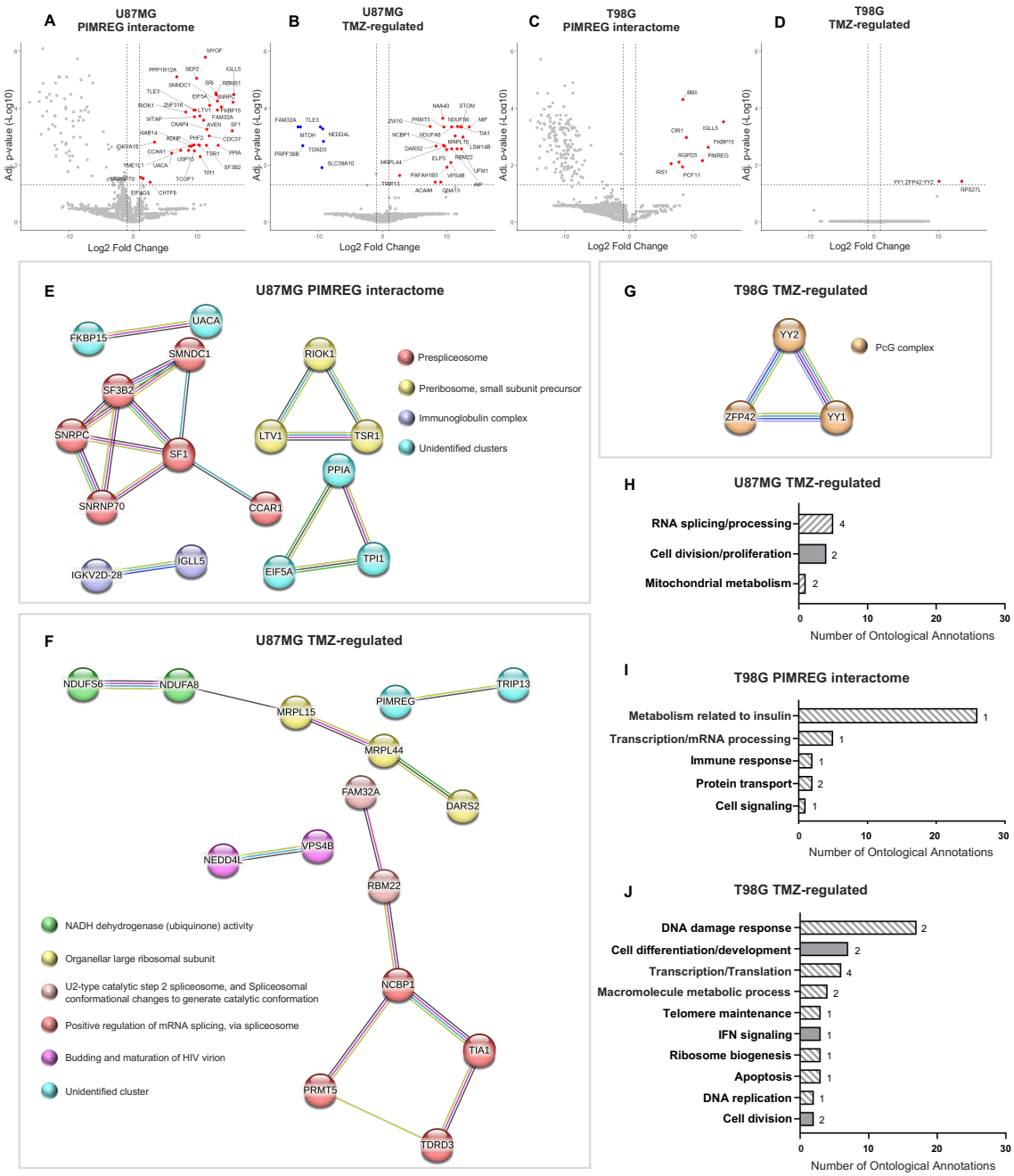

Fig. 2: PIMREG interactome of GBM cells treated with TMZ and vehicle (DMSO). (**A-D**) Volcano plot graphs of PIMREG interacting proteins in U87MG (A, B) and T98G (C, D) cells. (**B, D**) TMZ-regulated PIMREG interactors (TMZ vs. DMSO). Upregulated proteins (red dots) interact with PIMREG only under TMZ treatment or show increased association under treatment. Downregulated proteins (blue dots) exhibit reduced or lost binding upon TMZ treatment. (**A, C**) PIMREG interacting proteins under vehicle (DMSO) conditions (PIMREG IP vs. IgG). Proteins with adjusted p-value < 0.05 and $\log_2$ fold change > 1 (PIMREG IP vs. IgG) or $\log_2$ fold change < -1 and >1 (TMZ vs. DMSO) were considered significant (highlighted as blue or red dots). (**E**) Interaction network of proteins identified as PIMREG interactors in U87MG cells (PIMREG IP vs. IgG). (**F**) Interaction network of the proteins identified as TMZ-regulated PIMREG interactors

in U87MG and (**G**) in T98G cells. Each node represents one protein. The proteins interacting with each other are represented in clusters. Node colors indicate proteins that have the same function within the clusters. Lines connecting the nodes represent known interactions (cyan: from curated databases; magenta: experimentally determined), predicted interactions (green: gene neighborhood; red: gene fusions; blue: gene co-occurrence) and other types of interactions (black: co-expression; yellow: text mining; light blue: protein homology). (**H, I, J**) Biological processes (BP) in each group of PIMREG interacting proteins. Number of ontological terms grouped as a BP (graph bars) is depicted in the x axis. Number of genes involved in each BP is shown next to each bar. The bars in gray represent previously described functions of PIMREG. The hatched bars represent the putative new functions of PIMREG.

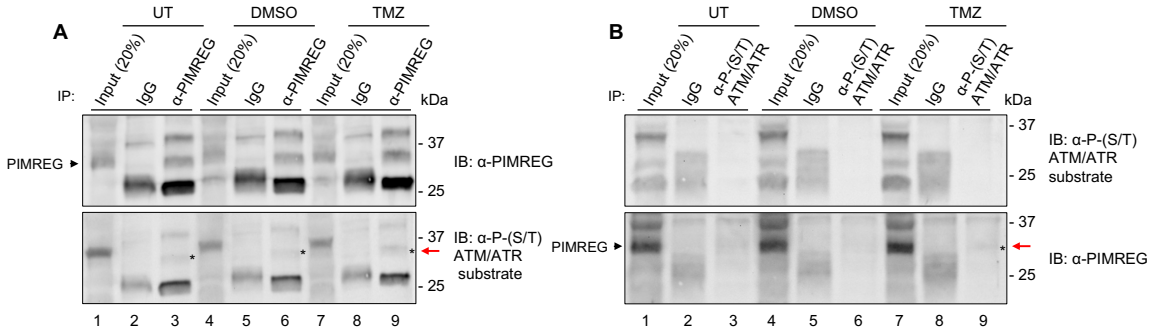

Fig. 3: PIMREG is a substrate of ATM/ATR. Lysates of T98G cells untreated (UT) or treated with TMZ and vehicle (DMSO) for 24 h were precipitated with (**A**) anti-PIMREG antibody and isotype control (IgG). Western blot analysis with anti-PIMREG antibody shows the precipitated protein in the upper panel. Precipitated PIMREG is indicated with the arrowhead (lanes 3, 6 and 9). Immunoblotting of the precipitated protein with anti-phospho-ATM/ATR substrate antibody is shown in the lower panel. Asterisks (*) indicate the precipitated PIMREG protein detected with the anti-phospho-ATM/ATR substrate antibody. (**B**) ATM/ATR substrates immunoprecipitated using anti-phospho-ATM/ATR substrate antibody were immunoblotted with the same antibody (upper panel) and anti-PIMREG antibody (lower panel). Asterisk (*) indicates the precipitated phospho-ATM/ATR substrates detected with anti-PIMREG antibody (lane 9). As input control, lanes 1, 4 and 7 were loaded with 20 % of the protein extract used for each precipitation reaction. UT: untreated.

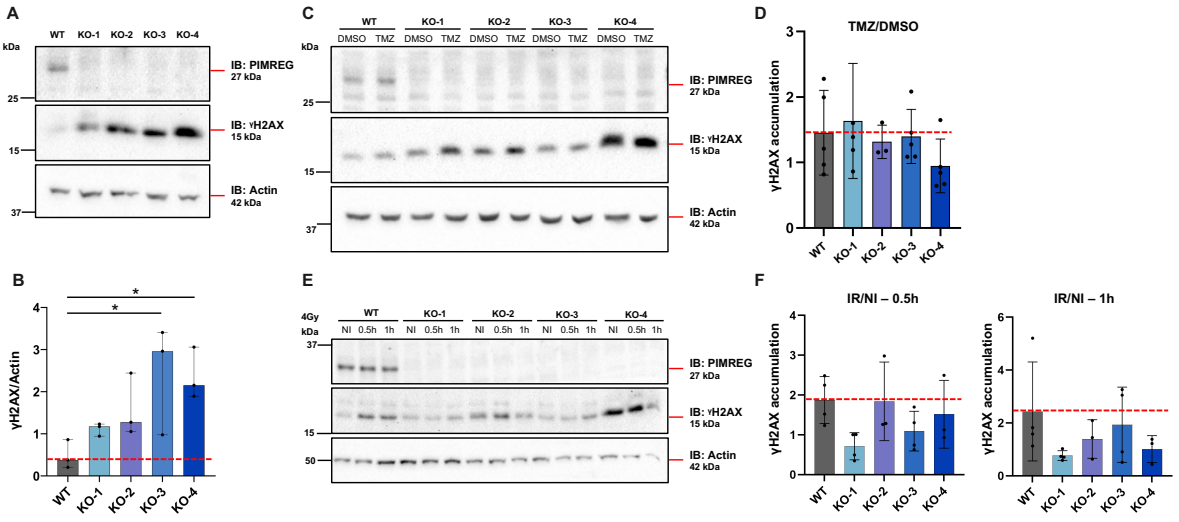

Fig. 4: γH2AX accumulation in PIMREG KO cells. (**A**) Western blot analysis of protein extracts from T98G WT and PIMREG KO (KO-1, KO-2, KO-3 and KO-4) cells. Membranes were blotted with anti-PIMREG, anti-phospho-H2AX (S139) antibodies. Actin was used as a loading control. (**B**) Bar graph showing densitometric quantification of γH2AX bands, normalized to their corresponding endogenous actin levels (γH2AX/actin). Results are shown as mean ± SD (standard deviation) of three independent experiments. Red dashed line indicates γH2AX levels in WT cells for comparison. (**C**) Western blot analysis of protein extracts derived from T98G WT and PIMREG KOs treated with TMZ or vehicle (DMSO) for 24 h. (**D**) Bar graph showing γH2AX accumulation expressed as the ratio of γH2AX levels (γH2AX/actin) in TMZ-treated cells relative to their corresponding DMSO control (TMZ/DMSO). Results are shown as mean ± SD (standard deviation) of five independent experiments. Red dashed line indicates the γH2AX accumulation in WT cells upon TMZ treatment. (**E**) Western blot analysis of protein extracts from T98G WT and PIMREG KO cells following IR exposure. Samples were collected at 0.5 and 1h post-irradiation. Tubulin was used as a loading control. (**F**) Bar graph showing γH2AX accumulation expressed as the ratio of γH2AX levels (γH2AX/tubulin) in IR-treated cells relative to their corresponding non-irradiated controls (IR/NI). Results are shown as mean ± SD (standard deviation) of four independent experiments. Red dashed line indicates γH2AX accumulation in WT cells following IR exposure. Representative western blots are shown. (*) p-value < 0.05, One-way ANOVA test.

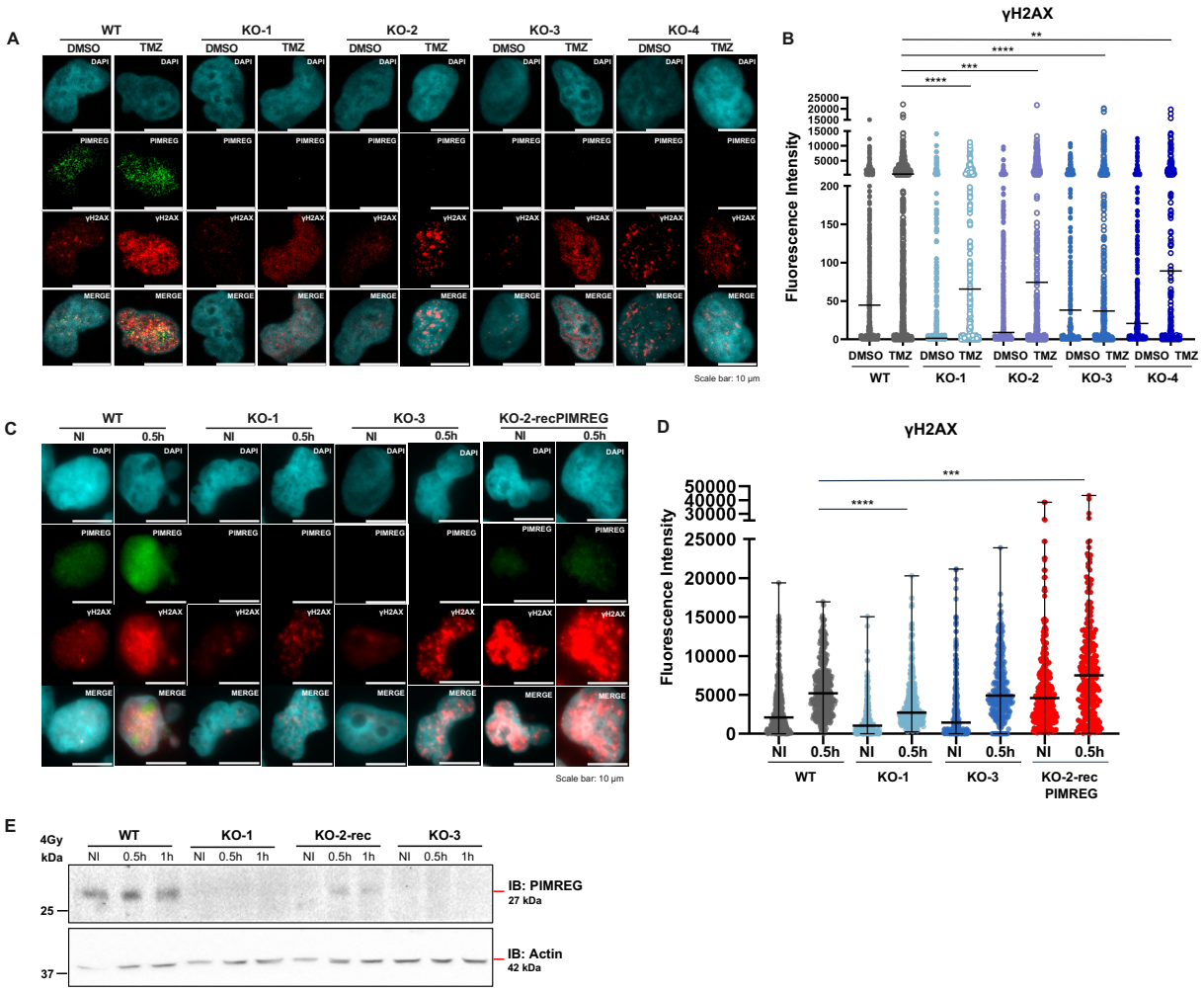

Fig. 5.: PIMREG deficiency impairs nuclear accumulation of γH2AX in GBM cells treated with genotoxic agents. Representative immunofluorescence analysis of T98G WT and PIMREG KO cells treated with (**A**) TMZ or vehicle (DMSO) for 24 h and (**C**) exposed to IR (4 Gy) and collected at 0.5 h post-irradiation. PIMREG is shown in green (Alexa Fluor 488), γH2AX in red (Alexa Fluor 555) and nuclei (DAPI) in cyan. Scale bar: 10 µM. (**B, D**) Fluorescence intensity quantification of nuclear γH2AX, quantified in at least 75 cells per condition. Data are from 3 to 5 independent experiments. The horizontal bars indicate the median intensity. (**) *p*-value < 0.01, (***) *p*-value < 0.001 and (****) *p*-value < 0.0001, One-way ANOVA test followed by the post-test Kruskal-Wallis was applied. WT: wild-type; KO: knockout; KO-2-recPIMREG: KO-2 cells that recovered PIMREG's expression; NI: non-irradiated. (**E**) Western blot analysis of PIMREG in the same samples in (C and D): T98G WT, PIMREG KOs (KO-1 and KO-3) and KO-2-recPIMREG. Membranes were blotted with anti-PIMREG and actin was used as a loading control.

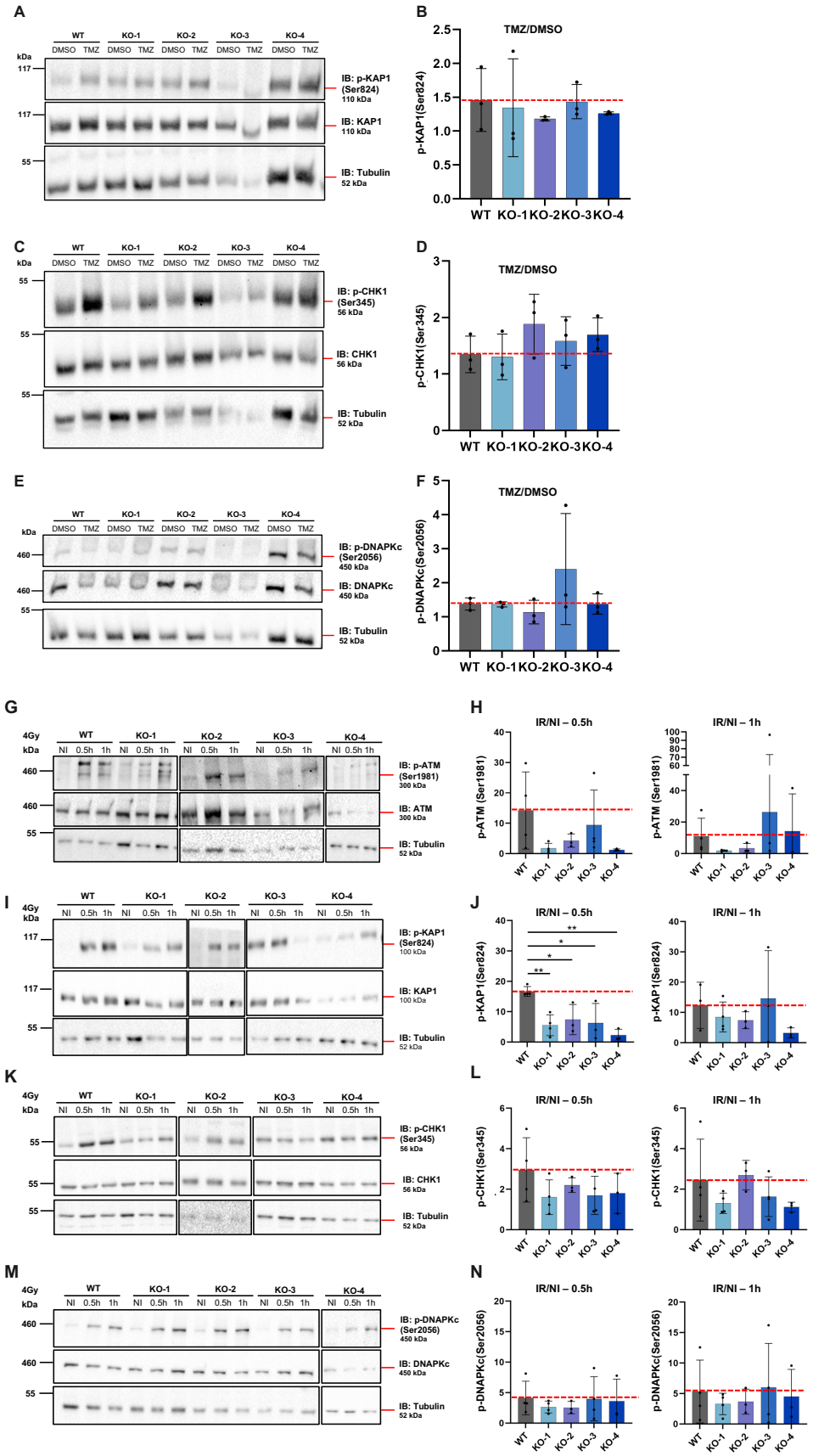
A
WT KO-1 KO-2 KO-3 KO-4
DMSO TMZ DMSO TMZ DMSO TMZ DMSO TMZ DMSO TMZ
kDa
117
117
55
IB: p-KAP1 (Ser824) 110 kDa
IB: KAP1 110 kDa
IB: Tubulin 52 kDa
B
TMZ/DMSO
p-KAP1(Ser824)
WT KO-1 KO-2 KO-3 KO-4
C
55
55
55
IB: p-CHK1 (Ser345) 56 kDa
IB: CHK1 56 kDa
IB: Tubulin 52 kDa
D
TMZ/DMSO
p-CHK1(Ser345)
E
460
460
55
IB: p-DNAPKc (Ser2056) 450 kDa
IB: DNAPKc 450 kDa
IB: Tubulin 52 kDa
F
TMZ/DMSO
p-DNAPKc(Ser2056)
G
4Gy
NI 0.5h 1h
IB: p-ATM (Ser1981) 300 kDa
IB: ATM 300 kDa
IB: Tubulin 52 kDa
H
IR/NI – 0.5h
IR/NI – 1h
p-ATM (Ser1981)
I
IB: p-KAP1 (Ser824) 100 kDa
IB: KAP1 100 kDa
IB: Tubulin 52 kDa
J
p-KAP1(Ser824)
K
IB: p-CHK1 (Ser345) 56 kDa
IB: CHK1 56 kDa
IB: Tubulin 52 kDa
L
p-CHK1(Ser345)
M
IB: p-DNAPKc (Ser2056) 450 kDa
IB: DNAPKc 450 kDa
IB: Tubulin 52 kDa
N
p-DNAPKc(Ser2056)

Fig. 6: PIMREG KO affects activation of DNA damage response signaling molecule following IR exposure. (**A, C, E**) Western blot analysis of protein extracts derived from T98G WT and PIMREG KOs treated with TMZ or vehicle (DMSO) for 24 h. Membranes were blotted with anti-Phospho-KAP1 (Ser824) and KAP1 (A), anti-Phospho CHK1 (Ser345) and CHK1 (C) and anti-Phospho-DNA-PKc (Ser2056) and DNA-PKc (E) antibodies. Tubulin was used as a loading control. (**B, D, F**) Bar graph showing densitometric quantification of phosphorylated protein band intensities normalized to total protein levels. Protein activation is expressed as the ratio of the phosphorylation levels in TMZ-treated cells relative to their corresponding DMSO control (TMZ/DMSO). Results are shown as mean ± SD (standard deviation) of three independent experiment. Red dashed line indicates the protein activation in WT cells upon TMZ treatment. (**G, I, K, M**) Western blot analysis of protein extracts from T98G WT and PIMREG KO cells (KO-1, KO-2, KO-3, and KO-4) following exposure to IR (4Gy). Samples were collected at 0.5 and 1h post-irradiation. Membranes were blotted with anti-Phospho ATM (Ser1981) and ATM (G), anti-Phospho-KAP1 (Ser824) and KAP1 (I), anti-Phospho CHK1 (Ser345) and CHK1 (K), anti-Phospho-DNA-PKc (Ser2056) and DNA-PKc (M) antibodies. Tubulin was used as a loading control. (**H, J, L, N**) Bar graph showing densitometric quantification of phosphorylated protein band intensities normalized to total protein levels. Protein activation is expressed as the ratio of the phosphorylation levels in IR samples relative to their corresponding non-irradiated controls (IR/NI). Results are shown as mean ± SD (standard deviation) of four independent experiment. Red dashed line indicates the protein activation in WT cells at the indicated time points following IR exposure. (*) p-value < 0.05 and (**) p-value < 0.01, One-way ANOVA test. WT: wild-type; KO: knockout; NI: non-irradiated.

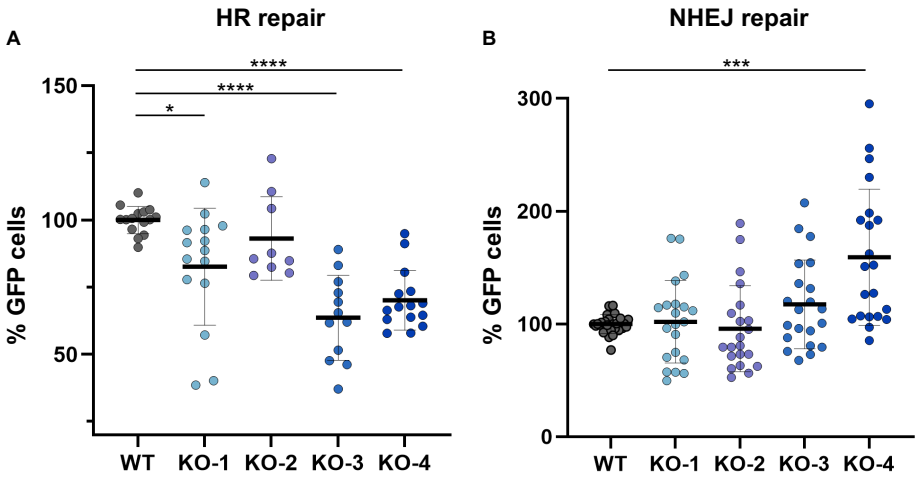

Fig. 7: DNA repair reporter assay. The graphs show the percentage of PIMREG WT and PIMREG KO (KO-1, KO-2, KO-3, and KO-4) cells that repaired the DSBs. GFP reports the repair events via (**A**) HR in U2OS DR-GFP and (**B**) NHEJ in HeLa EJ5-GFP cells. The percentage of GFP-positive cells was normalized to the mean percentage of WT control cells within each experiment. Experiments were performed at least three times in triplicates. Fifty thousand events were acquired. Sample sizes for HR repair (A): WT (n = 5), KO-1 (n = 5), KO-2 (n = 3), KO-3 (n = 4), KO-4 (n = 5). Sample sizes for NHEJ repair (B): WT (n = 9), KO-1, KO-2, KO-3 and KO-4 (n = 7). (*) *p*-value < 0.05, (***) *p*-value < 0.001 and (****) *p*-value < 0.0001, Brown-Forsythe and Welch ANOVA.